

# Probing reionization with Lyman $\alpha$ emission lines

Michael R. Santos<sup>\*</sup>

*Theoretical Astrophysics, California Institute of Technology, Mailcode 130-33, Pasadena, CA 91125, USA*

2 February 2008

## ABSTRACT

Lyman  $\alpha$  emission from high-redshift galaxies may be a powerful probe of the ionization history of the IGM at  $z > 6$ : the observed Lyman  $\alpha$  emission line is sensitive to the neutral fraction of IGM hydrogen in the range 0.1–1. We present calculations of observed Lyman  $\alpha$  emission lines from  $z > 6$  galaxies, illustrating the effect of varying the many free parameters associated with the emitting galaxy, its halo, and the IGM around the galaxy. In particular, we use a dynamic model of the IGM that includes the effect of IGM infall toward the emitting galaxy. Galactic winds may play a crucial role in determining observed Lyman  $\alpha$  line fluxes. We compare our model predictions with observations of two  $z = 6.5$  galaxies and conclude that, if galactic winds are allowed for, existing observations place no constraint on the neutral fraction of the IGM at  $z = 6.5$ . Future space-based observations will constrain the importance of galactic winds; if winds are unimportant for the observed  $z = 6.5$  galaxies, our models suggest that the IGM neutral fraction at  $z = 6.5$  is  $\lesssim 0.1$ .

**Key words:** line: profiles – intergalactic medium – galaxies: high-redshift – diffuse radiation – cosmology: theory.

## 1 INTRODUCTION

Strong Lyman  $\alpha$  emission is present in many distant galaxies, and is an important signpost for discovering high-redshift galaxies and, especially, measuring redshifts for them. The presence of strong Lyman  $\alpha$  emission has been crucial in confirming the highest redshift galaxies known at  $z > 5$  (e.g., Hu, McMahon, & Cowie 1999; Hu et al. 2002a,b; Ajiki et al. 2003; Kodaira et al. 2003; Rhoads et al. 2003). See Taniguchi et al. (2003) for a review. It also plays an important role in identifying the redshift of some galaxies at  $z \gtrsim 2$  because its strength, even in some apparently extremely dusty galaxies, allows for redshift determinations when little continuum light is visible (e.g., Steidel et al. 2003; Chapman et al. 2003).

In this paper we concentrate on Lyman  $\alpha$  emission powered by star formation. Hot stars emit photons capable of ionizing hydrogen. If the ionized gas density is sufficient, hydrogen will recombine on relevant timescales. The recombination cascade produces a rich spectrum of lines, but usually includes a Lyman  $\alpha$  photon (see Osterbrock 1989, for a review). Because most recombinations produce Lyman  $\alpha$  photons, it is predicted to be the strongest line emitted from recombination emission. AGN activity can also provide ionizing photons that ultimately generate a strong Lyman  $\alpha$  line. Additional sources of Lyman  $\alpha$  photons are atomic-hydrogen cooling of gas (e.g., Haiman, Spaans, & Quataert

2000; Fardal et al. 2001) and fluorescence of gas clouds illuminated by a strong, non-local source of ionization (e.g., Reuland et al. 2003).

The predicted strength of the Lyman  $\alpha$  line, and the assumed prevalence of star formation at early times (inferred from the abundance of old stars in the local universe) led to an early prediction of an abundant population of high-redshift galaxies with very strong Lyman  $\alpha$  emission lines (Partridge & Peebles 1967). Though subsequent revisions to the theory of galaxy formation, primarily that it was a hierarchical process, explained the relative lack of Lyman  $\alpha$  detections compared to those early predictions (Haiman & Spaans 1999), searching for galaxies based solely on strong Lyman  $\alpha$  emission has been validated recently as an effective technique for identifying galaxies up to  $z = 6.5$ .

Lyman  $\alpha$  is a resonant transition with a large cross-section. As a consequence, small quantities of neutral hydrogen scatter away Lyman  $\alpha$  photons in direction and frequency. In particular, if the intergalactic medium (IGM) is not highly ionized, as is expected for at least some of the time between recombination ( $z \sim 1100$ ) and  $z \simeq 6$  (Fan et al. 2002; Kogut et al. 2003), then the neutral hydrogen in the IGM can easily scatter the Lyman  $\alpha$  line from galaxies. The Lyman  $\alpha$  photons are not destroyed, but the scattering process diffuses the line in areal coverage and frequency (Loeb & Rybicki 1999), and the resulting low surface brightness emission is currently unobservable.

A simple consideration of the IGM shows that the blue side of the emergent Lyman  $\alpha$  line would be scattered away

<sup>\*</sup> E-mail: mrs@tapir.caltech.edu

by a neutral IGM, and only the red side of the line would be observed. This follows from considering that most of the scattering by neutral hydrogen comes at wavelengths near the Lyman  $\alpha$  transition in the rest-frame of the gas. However, for a completely neutral IGM at high redshifts, the Lyman  $\alpha$  cross-section far from resonance becomes important, since the natural line profile has ‘damping wings’ that fall off only like  $\nu^{\pm 2}$ . Thus even if the IGM has no component at the velocity of corresponding to resonant scattering of a particular Lyman  $\alpha$  photon, that photon may still be scattered. This observation led to the conclusion that observations of Lyman  $\alpha$  emission lines (or their absence) at high redshifts may probe the ionization state of the IGM in a regime poorly tested by the Gunn-Peterson trough measurements,  $x_{\text{HI}} \sim 1$  (Miralda-Escude 1998; Miralda-Escude & Rees 1998; Haiman 2002; Barkana & Loeb 2003b; Cen 2003b).

In particular, since the *WMAP* satellite discovered a high optical depth to the last scattering surface (Kogut et al. 2003), the ionization history of the universe at  $z > 6$  is of great interest. Though the *WMAP* results indicate that the universe was mostly ionized for a substantial history of the universe at  $z > 6$ , it does not constrain the exact ionization level or the history in detail. There are now many predictions for the ionization history at  $z > 6$  based on semi-analytic and numerical modelling of early star formation (e.g., Cen 2003a; Wyithe & Loeb 2003; Ciardi, Ferrara, & White 2003; Haiman & Holder 2003). If there is a population of strong Lyman  $\alpha$  emitters at the redshifts in question,  $6 \lesssim z \lesssim 20$ , and if the effect of IGM scattering on their observed properties can be calculated, then future surveys for Lyman  $\alpha$  emission may provide valuable information on the reionization history at  $z > 6$ .

Here we use a more sophisticated treatment of the dynamics of the IGM around galaxies with strong intrinsic Lyman  $\alpha$  emission to investigate the effect of the IGM on the observed line. The IGM model we use will be presented in more detail separately, but is summarized here and nearly identical to that described in Barkana (2002). The key feature is that infall of the IGM toward the galaxies is included. Barkana & Loeb (2003a) have showed that such an IGM model makes a prediction for an absorption feature in the spectra of high-redshift QSO Lyman  $\alpha$  lines. Here we consider normal galaxies, where the effect of an infalling IGM is even stronger.

Throughout this paper we assume a cosmology based on the recent results from *WMAP* and other work (Spergel et al. 2003, and references therein):  $\Omega_{\text{M}} = 0.3$ ,  $\Omega_{\Lambda} = 0.7$ ,  $H_0 = 70 \text{ km s}^{-1}$ , and  $\Omega_{\text{b}} = 0.0469$ . In general we quote distances in physical Mpc, denoted by ‘pMpc.’

This paper is organized as follows. In Section 2 we present the Lyman  $\alpha$  scattering cross-section. Section 3 describes the model for the intrinsic Lyman  $\alpha$  line profile and the observed profile modified by IGM scattering. Section 4 presents Lyman  $\alpha$  line profiles as a function of the (many) input parameters that influence the observed line profile. We introduce the possible role of galactic winds in Section 5. Section 6 discusses our Lyman  $\alpha$  flux predictions with comparison to current observations, and also reviews model assumptions. Section 7 summarizes.

## 2 LYMAN $\alpha$ SCATTERING

A Lyman  $\alpha$  photon is emitted when a hydrogen atom makes a transition from the  $n = 2$  level to the  $n = 1$  ground-state. The emitted photon has an energy of 10.199 eV and a wavelength of  $\lambda_{\alpha} = 1215.67 \text{ \AA}$ . The transition is the strongest spontaneous transition of a hydrogen atom, with an Einstein  $A$  value of  $A_{21} = 6.265 \times 10^8 \text{ s}^{-1}$ . Correspondingly, the absorption cross-section of the transition is relatively large as well.

A Lyman  $\alpha$  photon travelling through a region of neutral hydrogen will be repeatedly absorbed and re-emitted. This process by itself does not destroy Lyman  $\alpha$  photons, but if photons are scattered over a sufficiently large region such that an observation spatially resolves the emission, then the Lyman  $\alpha$  line will be difficult to observe in practice (Loeb & Rybicki 1999). In this work we assume that Lyman  $\alpha$  photons scattered in the IGM, that is, outside of the virial radius of the emitting galaxy, are missed by observation. For a  $z \gtrsim 6$  galaxy, the virial radius is larger than  $1''$  (the size of a typical spectroscopic slit) for any galaxy more massive than  $\sim 3 \times 10^9 M_{\odot}$ .

So under the assumption that photons emitted in the Lyman  $\alpha$  emission line of a galaxy are lost from subsequent observation if they are scattered by the IGM, we constructed a model of the IGM (see Section 3.2.1) and computed the absorption due to neutral hydrogen. The natural absorption cross-section  $\sigma_{\text{N}}$  is (Peebles 1993)

$$\sigma_{\text{N}}(\nu) = \frac{3\lambda_{\alpha}^2 A_{21}^2}{8\pi} \frac{(\nu/\nu_{\alpha})^4}{4\pi^2(\nu - \nu_{\alpha})^2 + (A_{21}^2/4)(\nu/\nu_{\alpha})^6}, \quad (1)$$

where  $\nu = c/\lambda$  and  $\nu_{\alpha} = c/\lambda_{\alpha}$ .

The total absorption cross-section due to a parcel of IGM gas is determined by the kinetic properties of the gas, both bulk and thermal, as well as the natural cross-section. Bulk motions just introduce a frequency shift, but thermal motions broaden the profile, modelled as the convolution of the natural cross-section with a Maxwellian velocity distribution,

$$\sigma_{\text{V}}(\nu) = \int_{-\infty}^{\infty} M(v) \sigma_{\text{N}}(\nu - \nu_{\alpha} v/c) dv, \quad (2)$$

$$M(v) = \left( \frac{m_{\text{H}}}{2\pi kT} \right)^{1/2} \exp \left( -\frac{m_{\text{H}} v^2}{2kT} \right), \quad (3)$$

where  $m_{\text{H}}$  is the mass of the hydrogen atom and  $T$  is the temperature of the IGM gas (modelled in the next section). For the usual Lorentzian approximation of  $\sigma_{\text{N}}$ , the convolved cross-section would be a Voigt profile, hence we label our convolved cross-section  $\sigma_{\text{V}}$ . Figure 1 shows  $\sigma_{\text{V}}(\lambda)$ , assuming a temperature of  $T = 10^4 \text{ K}$  for the scattering gas. The profile has a Doppler core with a half-width of  $\sim 10 \text{ km s}^{-1}$  and power-law tails called ‘damping wings.’ If the IGM at the redshift of interest is or has previously been reionized, then  $T = 10^4 \text{ K}$  is probably a good approximation. If the IGM is still thermally pristine, then the temperature may be as low as  $\sim 20 \text{ K}$ , resulting in a narrower Doppler core of the scattering profile. In practice this would have a small effect on any near-future observation.

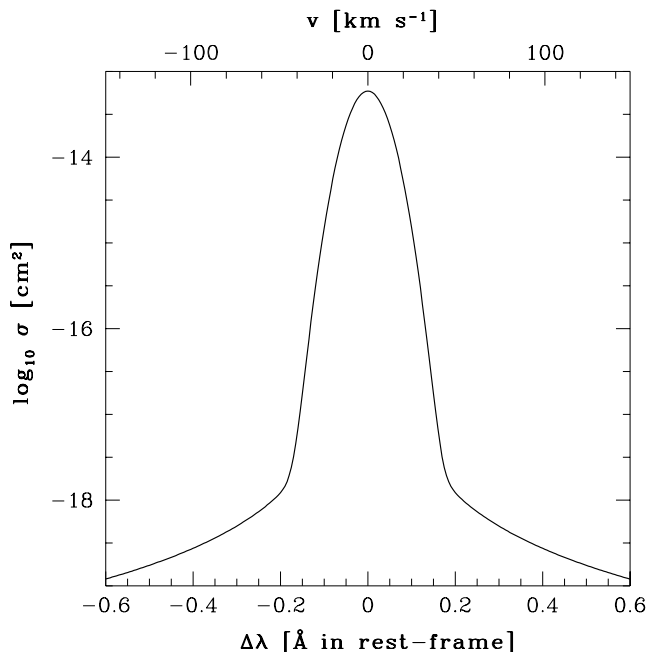


**Figure 1.** Cross-section for Lyman  $\alpha$  absorption, as a function of wavelength difference from resonance in the frame of the absorbing atom. The top axis shows the velocity (in the frame of the absorbing atom) where the Lyman  $\alpha$  resonance corresponds to the wavelength on the bottom axis.

### 3 LYMAN $\alpha$ LINE PROFILES

We will refer to two types of Lyman  $\alpha$  lines from galaxies. The **intrinsic line** is the line produced in the galaxy, specifically, the line that reaches the virial radius of the halo containing the emitting galaxy. The **observed line** is the line after propagation through the IGM to  $z = 0$ .

#### 3.1 Intrinsic Lyman $\alpha$ emission line

A Lyman  $\alpha$  emission line from a high-redshift galaxy is typically a consequence of hydrogen recombinations in nebular gas. The ionization of the H II region may be maintained either by hot stars or by gas accretion onto a black hole. Though luminous QSOs have been discovered at  $z > 6$  (Fan et al. 2003, and references therein), deep x-ray data indicates that most galaxies at those redshifts do not contain powerful AGNs (Barger et al. 2003). Thus in this work we will assume recent ( $\lesssim 10$  Myr ago) star formation powers Lyman  $\alpha$  emission lines.

Type O stars emit hydrogen-ionizing photons.<sup>1</sup> Some fraction,  $f_{\text{esc}}$ , of these photons may escape the galaxy without absorption. The rest of the photons are absorbed by either neutral hydrogen or dust within the galaxy. An ionizing photon absorbed by a hydrogen atom initiates a cascade of recombination emission, ultimately resulting in a Lyman  $\alpha$  photon about 2/3 of the time, and two-photon emission the other 1/3 of the time (Osterbrock 1989). A Lyman  $\alpha$  photon

<sup>1</sup> Approximately 1 Gyr after the onset of star formation hot white dwarfs form, and these may emit substantial ionizing radiation (Charlot & Fall 2000); however, for  $z \gtrsim 5.5$  the universe is not old enough to have formed these stars.

subsequently scatters through absorption and reemission until the optical depth of the galaxy at its wavelength is  $\lesssim 1$ ; the optical depth is determined both by the position and direction of the photon, and also its wavelength. If dust is present, it may absorb photons at any time in this process.

The radiative transfer problem for Lyman  $\alpha$  depends sensitively on the geometry of neutral hydrogen and dust within the galaxy (Neufeld 1991), and also the dynamics of the hydrogen (Kunth et al. 1998). For simplicity we will assume that the intrinsic Lyman  $\alpha$  emission line is centered at the systemic redshift of the emitting galaxy, with a Doppler profile shape described by a characteristic velocity,  $v_D$ ,

$$\phi_\nu^{\text{in}}(\nu) = \frac{1}{\sqrt{\pi}\Delta\nu_D} \exp \left[ \frac{-(\nu - \nu_\alpha)^2}{(\Delta\nu_D)^2} \right], \quad (4)$$

where  $\phi_\nu^{\text{in}}$  is the line profile per unit frequency and

$$\Delta\nu_D = \frac{v_D}{c} \nu_\alpha. \quad (5)$$

In Section 5 we address other possible intrinsic line profiles.

In this simplified model, two parameters characterize an intrinsic Lyman  $\alpha$  emission line: its luminosity,  $L_\alpha$ , and  $v_D$ .  $L_\alpha$  depends on the rate of production of ionizing photons,  $\dot{Q}$ , the ionizing photon escape fraction,  $f_{\text{esc}}$ , and dust absorption. The production of ionizing photons in turn depends on the star-formation rate and the metallicity and initial mass function (IMF) of the stars formed. None of these quantities may be reliably predicted from first principles for a galaxy at high redshift. Therefore, any use of the *observed* Lyman  $\alpha$  line of a high-redshift galaxy to deduce the radiative transfer properties of the IGM will be complicated, unless these quantities can be measured independently of the Lyman  $\alpha$  line.

The estimation of  $v_D$  is simpler. The likely minimum velocity scale for motion in a galaxy is the circular velocity of the parent halo,  $v_c$ ; this velocity may describe the gas motion if the star-formation is mediated by a violent process, such as the merging of two equal-mass galaxies. If star-formation is a more quiescent process in the galaxy, it may occur in a disk whose peak velocity is, roughly, between  $v_c$  and  $2v_c$ , for realistic halo and disk properties (Mo, Mao, & White 1998; Cole et al. 2000). Thus we assume  $v_c \lesssim v_D \lesssim 2v_c$ .

#### 3.2 Observed Lyman $\alpha$ emission line

The optical depth for photons to be absorbed in the IGM is

$$\tau(\nu) = \int_{R_{\text{vir}}}^{R_{\text{obs}}} x_{\text{HI}}(r) n_{\text{H}}(r) \sigma_{\text{V}}(\nu') dr, \quad (6)$$

$$\nu' = \nu \left[ 1 + \frac{v(r)}{c} \right], \quad (7)$$

where  $R_{\text{obs}}$  is the physical distance to the observer (though there is almost no contribution from  $r \gg R_{\text{vir}}$  because the Hubble flow eventually redshifts the IGM Lyman  $\alpha$  resonance far from the emitted Lyman  $\alpha$  line [in the frame of the galaxy]). We describe our model for  $n_{\text{H}}(r)$ ,  $v(r)$  and  $x_{\text{HI}}(r)$  in Section 3.2.1.

The observed Lyman  $\alpha$  emission line, in the rest-frame of the emitting galaxy, is then

$$\phi_\nu^{\text{obs}}(\nu) = \phi_\nu^{\text{in}}(\nu) \exp[-\tau(\nu)]. \quad (8)$$

### 3.2.1 IGM model

**3.2.1.1 Density and velocity** We will present a full description of our model for the density and velocity of IGM material in another paper (Santos & Adelberger, in preparation). The model is very similar to one described in Barkana (2002). Here we summarize our model as it applies to this paper.

The evolution of the density and velocity of the IGM follow from the small, linear, initial perturbations imprinted on the universe at very high redshift. We model the IGM starting from the statistical description of linear perturbations by applying a simple description of the non-linear evolution of the perturbations.

Specifically, we start by considering a Lyman  $\alpha$  emitting galaxy in a halo of total mass  $M$  at redshift  $z$ . We then constrain the initial linear overdensity on the scale of  $M$  to produce the halo at redshift  $z$ . Starting from that initial linear overdensity constraint, we use the excursion set formalism (Bond et al. 1991; Lacey & Cole 1993) to compute the mean<sup>2</sup> initial linear overdensities, averaged in spheres centered on the location of the halo, on scales larger than the scale of  $M$ . The mean initial linear overdensity decreases monotonically with increasing scale; this is not externally imposed. Our approach also implies that the halo is not substructure of a larger collapsed halo (see also Barkana 2002).

Once we have the initial linear overdensities of spheres enclosing the halo, we evolve those overdensities using the spherical top-hat model (Partridge & Peebles 1967). Because the mean initial linear overdensity decreases monotonically with increasing scale, there is no shell crossing, and the evolution of each IGM matter shell is independent of the evolution of the other shells.

Our dynamical evolution treats all matter equally, and we assume the baryons trace the dark matter in these shells. This description would be inappropriate if, e.g., the Lyman  $\alpha$  emitting galaxy blows a strong wind into its surrounding IGM (see Adelberger et al. 2003, for evidence of this at  $z = 3$ ), and we will return to this in Section 5.

A realistic distribution of initial linear overdensities around a halo, in contrast to the mean initial linear overdensities averaged over many halos, would not in general be spherically symmetric or even monotonic with radius within spherically-averaged shells. In addition to collapsing toward the galaxy, there would be structures collapsed and collapsing within the ‘IGM.’ The most straightforward way to assess the effect of these complicated dynamics would be with numerical simulation. Here we appeal to analytic results to demonstrate the effect of structure with the collapsing IGM will not severely affect our conclusions.

Scannapieco & Barkana (2002) computed the bivariate probability distributions of two halos forming at different positions. Their results suggest that outside the virial radius of a halo, the typical enhancement in the number density of halos is, at maximum, only a factor of a few, for any mass. Thus we conclude that the fraction of matter collapsed into halos (above a given mass) in the IGM surrounding our galaxy of interest is at most a few times the universal collapse fraction. At  $z = 6$  up to half the mass of the IGM may be in the form of collapsed halos with virial temperatures

above  $10^4$  K, that is, halos massive enough to collisionally ionize their hydrogen. That fraction decreases with increasing radius. The enhancement is also a decreasing function of decreasing mass. Thus we conservatively expect that our simple picture gives at most a factor of two overestimate of the optical depth, averaged over a reasonable sample of halos. At large optical depths, this error doesn’t affect the observed Lyman  $\alpha$  line properties, and at low optical depths we may underestimate the observed line by up to that same factor of two.

The practical output of our model is, given a halo mass  $M$  at redshift  $z$ , the radius, velocity, and mass of shells of IGM matter surrounding the galaxy from its virial radius to a large radius.

**3.2.1.2 Ionization state** To calculate the scattering of a Lyman  $\alpha$  emission line by the IGM, we need to know the ionization state of the hydrogen, in addition to its density and velocity profile. We solve the ionization balance of the IGM gas assuming two possible contributions, direct ionization by the galaxy emitting the Lyman  $\alpha$  line and, if the universe is ionized, a mean ionizing background.

After calculating the density distribution around a halo using the prescription described in the previous section, we solve the ionization balance as a function of distance from the galaxy. In general, the recombination rate of ionized hydrogen in the IGM is relatively small. As a consequence, in the pre-reionized universe H II regions around galaxies are not in equilibrium, but began growing when star-formation turned on and expand at the rate that ionizing photons can ionize more neutral IGM (rather than balancing recombinations within the ionized region). The H II region is still expected to have a relatively sharp boundary, as the mean free path of ionizing photons in the neutral IGM is small. After reionization, all of the IGM is highly ionized by the mean ionizing background, but the direct ionizing flux of the galaxy provides an additional proximity effect on the ionization balance immediately around it.

We divide the IGM around into one or two regions: either the universe is reionized, in which case all of the IGM is ionized; or the universe is not reionized, in which case there is an H II region in the IGM immediately surrounding the galaxy, and the IGM is fully neutral outside of that region. In that case the radius  $R_S$  of the H II region is calculated by solving

$$\int_{R_{\text{vir}}}^{R_S} \frac{4\pi r^2 n_H(r)}{\dot{Q} - \Lambda(r)} dr = t_{\text{SF}}, \quad (9)$$

$$n_H(r) = \frac{[\delta(r) + 1] \rho_{\text{H},0}(1+z)^3}{m_H}, \quad (10)$$

$$\dot{Q} = \int_{\nu_0}^{\infty} \frac{L_\nu}{h\nu} d\nu, \quad (11)$$

$$\Lambda(r) = \int_{R_{\text{vir}}}^r 4\pi \tilde{r}^2 n_H^2(\tilde{r}) \alpha_B(T) d\tilde{r}, \quad (12)$$

where  $R_{\text{vir}}$  is the virial radius of the galaxy’s halo,  $t_{\text{SF}}$  is the age of the star-formation activity<sup>3</sup>,  $\delta(r)$  is the overdensity with respect to the mean IGM density (calculated with the

<sup>2</sup> i.e., averaged over a large ensemble of identical halos

<sup>3</sup> We model star formation with a constant rate for an age  $t_{\text{SF}}$ .

model in the previous section),  $\rho_{\text{H},0}$  is the comoving (i.e.,  $z = 0$ ) density of hydrogen,  $z$  is the redshift of the galaxy,  $h\nu_0$  is the ionization energy of hydrogen,  $L_\nu$  is the specific luminosity of the galaxy, and  $\alpha_{\text{B}}(T)$  is the hydrogen Case B recombination coefficient. Since the H II region is almost completely ionized, here we assumed the electron physical density,  $n_{\text{e}}$ , is  $n_{\text{e}} = n_{\text{H}}$ , and ignored the contribution to  $n_{\text{e}}$  from helium. We have not included a clumping factor modification to the recombination rate; however, we do account for the mean overdensity of the IGM matter. Additional clumping of this material would decrease the size of the true H II region compared to our calculation.

The ionization rate for a hydrogen atom within an ionized region a distance  $r$  from the galaxy is

$$\Gamma(r) = \int_{\nu_0}^{\infty} \left( \frac{L_\nu}{4\pi r^2} + 4\pi J_\nu \right) \frac{\sigma_{\text{v}}(\nu)}{h\nu} d\nu, \quad (13)$$

where  $J_\nu$  is the mean specific intensity of the intergalactic background radiation. If the universe is not reionized, then we set  $J_\nu = 0$ . The hydrogen neutral fraction at any radius,  $x_{\text{HI}}(r)$ , is solved for by setting  $\Gamma(r)$  equal to the recombination rate at that radius,

$$x_{\text{HI}}(r) = 1 + \frac{\chi}{2} - \frac{1}{2} (\chi^2 + 4\chi)^{1/2} \quad (14)$$

$$\chi = \frac{\Gamma(r)}{n_{\text{H}}(r)\alpha_{\text{A}}(T)}, \quad (15)$$

where  $\alpha_{\text{A}}(T)$  is the hydrogen Case A (total) recombination coefficient. Additional clumping of the IGM would decrease  $\chi$  linearly, increasing  $x_{\text{HI}}$ .

We assume that when IGM gas falls across the virial radius it shocks and ionizes completely, and has no impact on the Lyman  $\alpha$  line profile.

## 4 LYMAN $\alpha$ LINE RESULTS

As described in Section 3.1, the strength and shape of the intrinsic Lyman  $\alpha$  emission line depends on many properties of the source galaxy. Additionally, the properties of the observed line are strongly modified by scattering in the IGM, which depends on the properties of the galaxy, its halo, and the IGM model. To illustrate these dependencies, we will adopt a fiducial model for a Lyman  $\alpha$  emitting galaxy, then show the dependence of the intrinsic and observed Lyman  $\alpha$  line on the properties of that galaxy and the IGM.

### 4.1 Fiducial galaxy/halo model

Our fiducial Lyman  $\alpha$  emitter model is a galaxy at rest in the center of a  $10^{11} \text{ M}_\odot$  halo at  $z = 6.5$ . ‘Fiducial galaxy’ will refer to this total system, galaxy plus halo. We assign the fiducial galaxy a constant star-formation rate (SFR) of  $10 \text{ M}_\odot \text{ yr}^{-1}$  for an age of  $t_{\text{SF}} = 10^8 \text{ yr}$ . The virial radius of the halo is  $R_{\text{vir}} = 19.8 \text{ kpc}$ , and the circular velocity at the virial radius is  $v_{\text{c}} = 148 \text{ km s}^{-1}$ . The halo dynamical time is then  $1.3 \times 10^8 \text{ yr}$ . Given our cosmology, and assuming the universal baryon to dark matter ratio holds in the halo, the halo contains  $1.5 \times 10^{10} \text{ M}_\odot$  of baryons. Thus at  $10 \text{ M}_\odot \text{ yr}^{-1}$  the gas supply could last up to  $1.5 \times 10^9 \text{ yr}$ , about twice the age of the universe at that redshift. The chosen SFR also

implies that 9 per cent of the baryons are converted into stars per halo dynamical time.

We use the following prescription to convert the fiducial galaxy properties into the emitted Lyman  $\alpha$  line. We convert the SFR to a hydrogen-ionizing photon luminosity using

$$\dot{Q} = 3.5 \times 10^{53} \text{ s}^{-1} \left( \frac{\text{SFR}}{\text{M}_\odot \text{ yr}^{-1}} \right), \quad (16)$$

appropriate for a Salpeter IMF from 1 to  $100 \text{ M}_\odot$  with 1/20th solar metallicity (Leitherer et al. 1999; Schaerer 2003). We assume that 2/3 of the ionizing photons that do not escape are converted into Lyman  $\alpha$  photons (Osterbrock 1989), so that

$$L_\alpha = \frac{2}{3}(1 - f_{\text{esc}})\dot{Q}h\nu_\alpha. \quad (17)$$

Note that this assumes there is no absorption by dust; we return to the issue of dust in Section 6.3. The other Lyman  $\alpha$  line parameter that needs to be specified is the line width, characterized by  $v_{\text{D}} \equiv f_{\text{v}}v_{\text{c}}$ . For our fiducial model, we set  $f_{\text{v}} = 1.5$ .

Additionally we need to model the effect of photoionization of the galaxy on the surrounding IGM. We assume the escaping photon luminosity of ionizing photons is simply

$$\dot{Q}_{\text{esc}} = f_{\text{esc}}\dot{Q}. \quad (18)$$

Our baseline choice for the escape fraction is  $f_{\text{esc}} = 0.1$ , giving

$$L_\alpha = 3.4 \times 10^{42} \text{ erg s}^{-1} \left( \frac{\text{SFR}}{\text{M}_\odot \text{ yr}^{-1}} \right). \quad (19)$$

### 4.2 IGM model dependence

Now we illustrate the IGM scattering of the Lyman  $\alpha$  line emitted by our fiducial galaxy, highlighting the importance of using our dynamic IGM model. At  $z = 6.5$ , the ionization state of the IGM is unknown. Limits from QSO spectra at redshifts approaching 6.5 indicate that  $x_{\text{HI}} > 10^{-3}$  averaged over the volume of the IGM, and  $x_{\text{HI}} > 10^{-2}$  averaged over the mass of the IGM (Fan et al. 2002). Simulations of reionization suggest that the  $z \sim 6$  transition from  $x_{\text{HI}} \simeq 1$  to  $x_{\text{HI}} \simeq 0$  was very sudden (Gnedin 2000). Combined with the QSO observations, these suggest that  $x_{\text{HI}}$  could have almost any value at  $z = 6.5$ . The *WMAP* results constrain the IGM ionization fraction to be  $\sim 1$  over a substantial fraction of the evolution of the universe at  $z > 6$ , but do not provide detailed constraints on models of  $x_{\text{HI}}(z)$ .

We start by assuming our fiducial galaxy ( $z = 6.5$ ) is embedded in a fully neutral IGM. Haiman (2002) argued that the detection of reasonably strong Lyman  $\alpha$  emission from  $z = 6.5$  galaxies did not rule out a fully neutral IGM, as had been previously suggested (Hu et al. 2002a; Rhoads et al. 2003). However, the calculations of Haiman (2002) did not account for the infall profile of the IGM around a  $z = 6.5$  galaxy.

First we illustrate the difference between our model of the IGM, and a smooth, Hubble flow model. We call our model the **dynamic IGM model** because we allow the IGM to evolve away from the comoving solution. We call the mean-density, comoving model the **simple IGM model**. The simplest difference between the models is the density

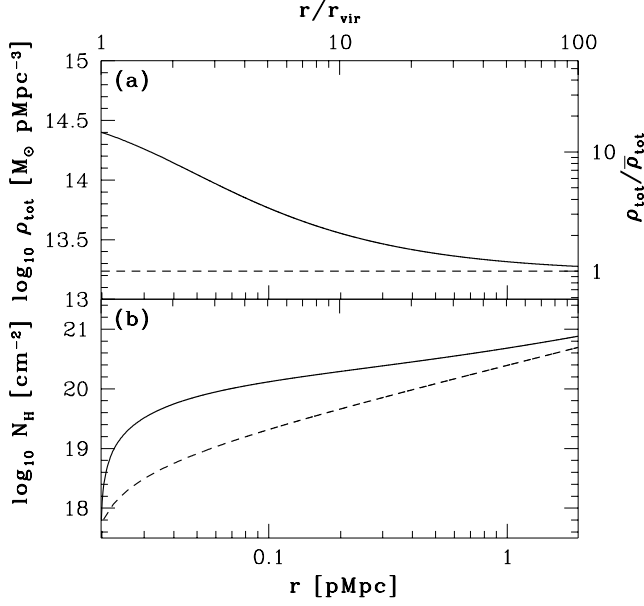


**Figure 2.** IGM density as a function of radius from the fiducial galaxy. The left edges of the plots are at the virial radius. (a) The total IGM mass density and density contrast as a function of radius in physical Mpc. (b) The cumulative IGM hydrogen column density to radius  $r$ . In both plots the solid curve is for the dynamic IGM model and the dashed curve is for the simple model.

of the IGM as a function of distance from the center of the halo. Figure 2a shows the density and density contrast of the IGM outside the halo virial radius for our dynamic IGM model, and a simple IGM. Within about 10 virial radii, or 0.2 physical Mpc (pMpc), the density enhancement is between 2 and 10 times the mean IGM density. Integrating the density out from the virial radius gives the curves shown in Fig. 2b, after converting total density to hydrogen density. Though Fig. 2 shows that there is a substantial difference in the density profile at small radius, the increased density as a function of radius is not the most important effect of the dynamic IGM model.

The most important difference between the IGM models, with respect to scattering of Lyman  $\alpha$  line photons, is the distribution of density as a function of velocity. Figure 3 shows the relationship between radius and velocity, for the dynamic and simple IGM models. With this relation we replot the densities of Fig. 2 against velocity in Fig. 4. The local Hubble parameter is  $H(z = 6.5) = 790 \text{ km s}^{-1} \text{ pMpc}^{-1}$ . For the IGM at positive velocities with respect to the galaxy, that is, the blue side of the line, there is little difference in density between the dynamic and simple models. However, while the simple model has no gas at negative velocities, corresponding to the red side of the line, the dynamic model has reached a column density of hydrogen of  $10^{20} \text{ cm}^{-2}$  by the time the velocity has reached 0. The absorption profile (Fig. 1) has a cross-section of greater than  $5 \times 10^{-14} \text{ cm}^2$  over the central  $10 \text{ km s}^{-1}$ . Thus the average optical depth within about  $100 \text{ km s}^{-1}$  of the red side of the line is greater than  $5 \times 10^4 x_{\text{HI}}$ . Immediately we can see that for  $x_{\text{HI}} \sim 10^{-5}$ , a typically expected value for the IGM, optical depths of order unity and greater may be expected. This optical depth on the red side of the observed line due to scattering by highly

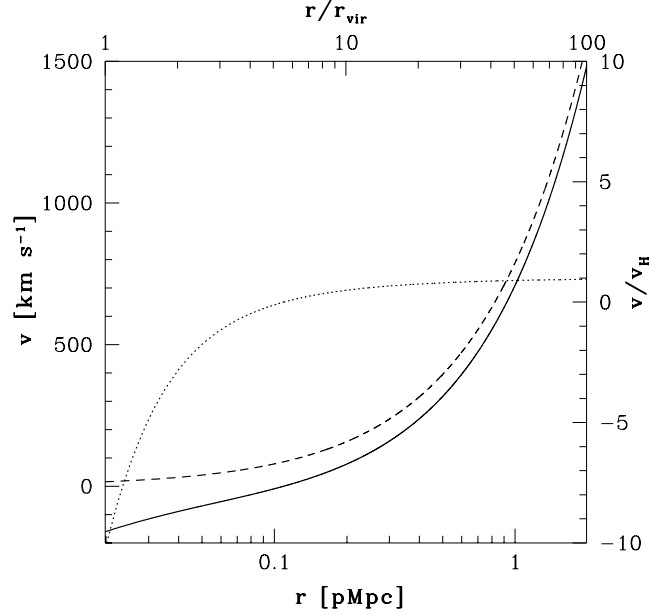


**Figure 3.** Velocity of IGM gas as a function of radius from the fiducial galaxy. The solid curve is the dynamic IGM model; the dashed curve is the Hubble flow relation of the simple model. The dotted curve is the ratio of the dynamic model to the simple model, in units marked on the right axis.

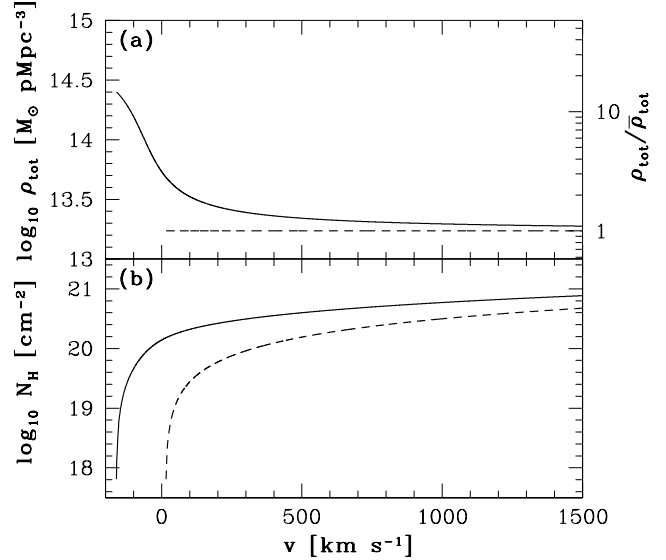


**Figure 4.** IGM density as a function of velocity in the frame of the fiducial galaxy. (a) The total IGM mass density and density contrast as a function of velocity. (b) The cumulative IGM hydrogen column density to velocity  $v$ . In both plots the solid curve is for the dynamic IGM model and the dashed curve is for the simple model.

(but not completely) ionized gas gives rise to a line profile distinctly different from a simple IGM model.

Figure 5 presents a schematic illustration of the difference between the dynamic and simple IGM models. As described above, we see that the dynamic model has gas with negative velocity, in contrast to the strictly positive velocity IGM in the simple model. We also see that the Stromgren

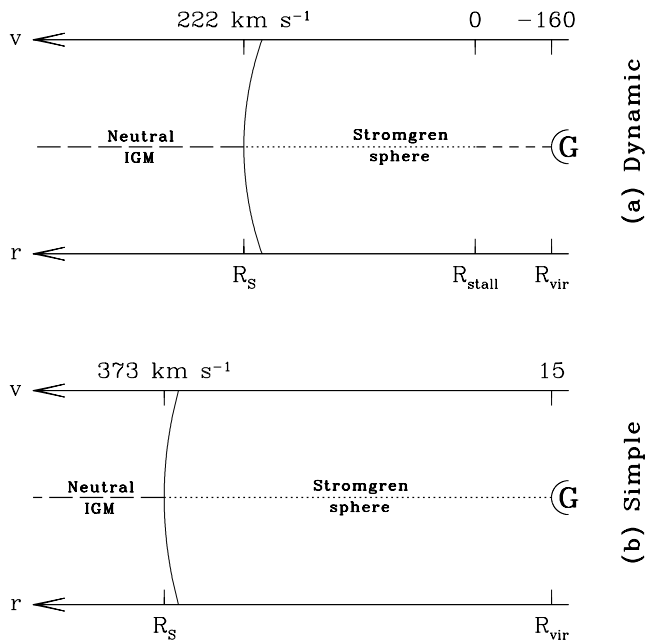


**Figure 5.** Schematic diagram of location and velocity of the IGM around the fiducial galaxy. (a) Dynamic IGM model. (b) Simple model. The galaxy is marked by a ‘G’ at right. The curve immediately surrounding it shows the virial radius of the halo. The next curve, at  $R_S$ , shows the Stroomgren sphere. The velocity axis marks the velocities (in  $\text{km s}^{-1}$ ) corresponding to these radii. In (a)  $R_{\text{stall}}$ , the radius where IGM gas has zero velocity with respect to the galaxy, is also marked. The dashed and dotted lines key the physical location of the IGM material to the contribution it makes to the scattering optical depth, shown in Fig. 6.

radius is both larger and extends to larger IGM velocities. In Fig. 5 we have keyed different physical regions with different line types; Fig. 6 shows the effect each of these regions has on the observed line profile.

In Fig. 6 we show the optical depth as a function of observed wavelength, subdivided by the velocity of the IGM gas responsible for the optical depth, for the fiducial galaxy with the dynamic and simple IGM models. We label the velocity of the IGM at radius  $r$  from the galaxy  $v(r)$ ;  $v(R_S) = 222 \text{ km s}^{-1}$  for the dynamic model, and  $v(R_S) = 373 \text{ km s}^{-1}$  for the simple model. When examining the observed line profile at a particular wavelength  $\lambda$ , it is useful to define the velocity in the frame of the galaxy where the Lyman  $\alpha$  resonance corresponds to that wavelength,

$$v_\alpha = c \left[ 1 - \frac{\lambda}{(1+z)\lambda_\alpha} \right]. \quad (20)$$

The total optical depth has three prominent regions. At  $v_\alpha > v(R_S)$ , the optical depth is dominated by Doppler core scattering from neutral IGM at  $v \simeq v_\alpha$ . At  $v(R_{\text{vir}}) < v_\alpha < v(R_S)$  the optical depth is still due to Doppler core scattering, but the IGM at  $v \simeq v_\alpha$  is mostly ionized. The third region is at  $v_\alpha < v(R_{\text{vir}})$ , where the optical depth is due to IGM gas at  $v > v(R_S)$  (the same as the first region), but now the scattering results from the damping wing of the scattering cross-section. Figure 6 illustrates that the central part of the observed line profile depends on the ionization state of the IGM gas in the Stroomgren sphere, and the red

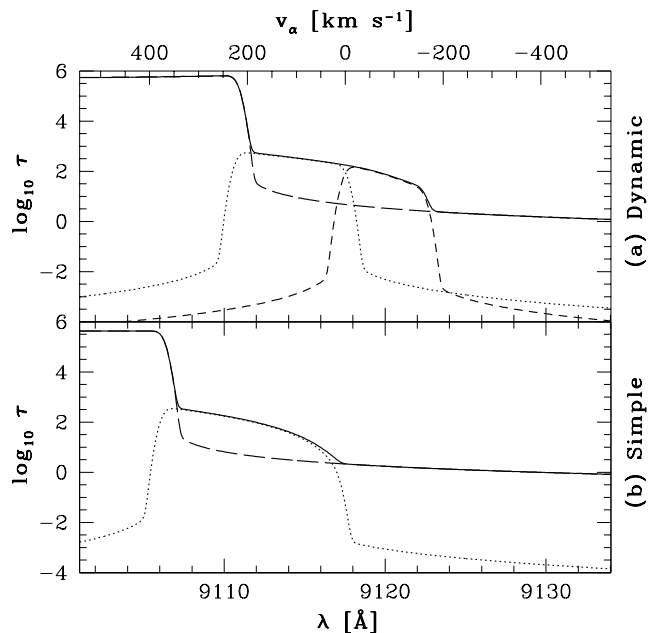


**Figure 6.** Optical depth due to IGM scattering as a function of observed wavelength. (a) Dynamic IGM model. (b) Simple model. The solid curves are the total optical depth due to all IGM H I. The short-dashed curves are the optical depth due to gas with negative velocity (in the frame of the galaxy). The dotted curves are the optical depth due to gas with positive velocity inside the Stroomgren sphere. The long-dashed curve is the optical depth due to gas outside the Stroomgren sphere.

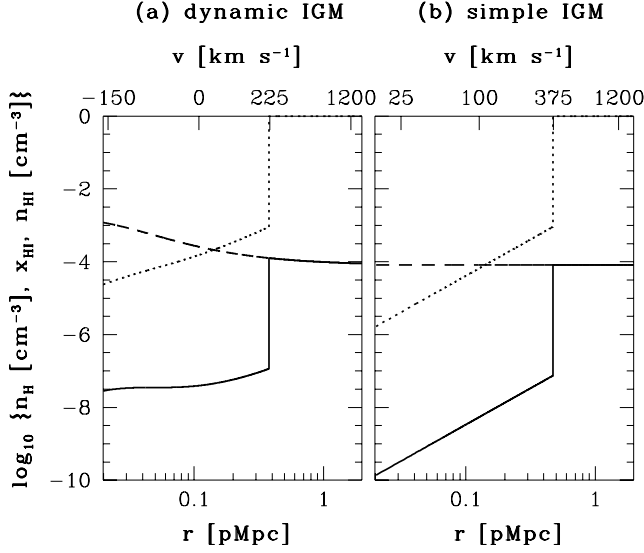
wing of the line profile depends on the size of the Stroomgren sphere and the IGM outside of it.

Figure 7 quantitatively compares the IGM density computed for both the dynamic and simple IGM models. In the dynamic model,  $R_S = 0.38 \text{ pMpc}$ , versus  $R_S = 0.47 \text{ pMpc}$  for the simple model. The larger Stroomgren sphere in the simple model is a consequence of the lower IGM density.

Figure 8 shows the observed Lyman  $\alpha$  line profiles per unit wavelength,  $\phi_\lambda$ , for the dynamic (solid curve) and simple (dashed curve) IGM models, compared to the intrinsic line profile (dotted curve) of the fiducial galaxy. The line profiles are plotted against observed wavelength and also  $v_\alpha$ .

For both the dynamic and simple models, the IGM outside of the virial radius, though highly ionized out to the Stroomgren radius, has sufficient optical depth to completely suppress the Lyman  $\alpha$  line with resonant scattering from the Doppler core of the absorption cross-section. Thus the wavelength range over which the line is completely suppressed corresponds to  $v_\alpha \gtrsim v(R_{\text{vir}})$ , where  $v(R_{\text{vir}})$  is the velocity of the IGM at the virial radius. For the dynamic model  $v(R_{\text{vir}}) = -160 \text{ km s}^{-1}$ , in contrast to  $15 \text{ km s}^{-1}$  for the simple model.

Because IGM gas is assumed to ionize completely as it crosses the virial radius, the line redward of  $v(R_{\text{vir}})$  is not scattered by the Doppler core of the absorption profile of any IGM gas. However, the observed lines are still depressed compared to the intrinsic profile at  $v_\alpha < v(R_{\text{vir}})$  due to scattering by the fully neutral IGM outside the Stroomgren sphere, via the red damping wing of the absorption cross-section. In summary, the optical depth at some wave-



**Figure 7.** Density and ionization state of the IGM as a function of radius and velocity. (a) Dynamic IGM model. (b) Simple model. The dashed curves are  $n_{\text{H}}$ , the total (H I + H II) hydrogen number density; the dotted curves are  $x_{\text{HI}}$ , the neutral hydrogen fraction; and the solid curves are  $n_{\text{HI}} \equiv x_{\text{HI}} n_{\text{H}}$ . Both plots are for the fiducial galaxy with radius in physical Mpc and velocity in the frame of the galaxy.

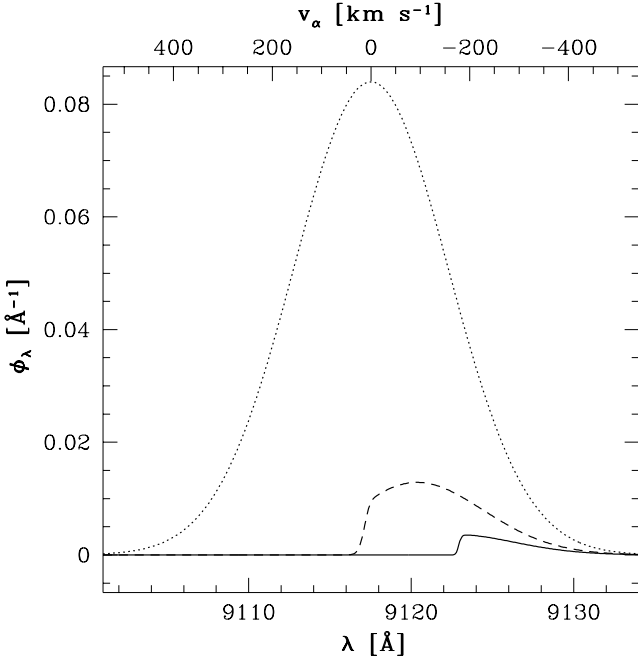


**Figure 8.** Lyman  $\alpha$  line profiles. The dotted curve is the intrinsic Lyman  $\alpha$  line profile of the fiducial galaxy. The solid curve is the observed Lyman  $\alpha$  line profile using the dynamic IGM model. The dashed curve is the observed line using the simple IGM model. The velocity where the Lyman  $\alpha$  resonance corresponds to the wavelength on the bottom axis is shown as  $v_{\alpha}$ , on the top axis.

length (and thus  $v_{\alpha}$ ) can be thought of as a sum of the optical depth due to Doppler core scattering by IGM gas at  $v = v_{\alpha}$ , and optical depth due to damping wing scattering by IGM gas at  $v \geq v(R_{\text{S}})$ . In Fig. 8, the difference between the dynamic and simple model predictions at  $v_{\alpha} = -100 \text{ km s}^{-1}$  is primarily a consequence of the presence of neutral gas at  $v = -100 \text{ km s}^{-1}$  in the dynamic model. At  $v_{\alpha} = -300 \text{ km s}^{-1}$ , the difference is entirely a consequence of neutral gas between  $+225$  and  $+375 \text{ km s}^{-1}$  (the velocity range over which the IGM is neutral in the dynamic model but ionized in the simple model).

The integrated observed line flux for the dynamic model is only 1.6 per cent of the intrinsic line, compared to 11 per cent for the simple model. Thus incorporating a dynamic model for the IGM is an important consideration in connecting theoretical predictions for Lyman  $\alpha$  emitters into observed counts, and for interpreting the ionization state of the IGM through Lyman  $\alpha$  emission line observations.

### 4.3 Galaxy/halo parameter dependence

In the previous section we showed that our dynamic IGM model has a substantial impact on the observed Lyman  $\alpha$  line from a galaxy at high redshift. In this section we illustrate how the observed line depends on properties of the galaxy and its halo. The parameters we explore are the halo mass, galaxy star-formation rate, age of star formation, escape fraction of ionizing radiation, and relation between the velocity width of the emitted line and the halo circular velocity. All figures are for the dynamic IGM model only; varying the parameters would have analogous effects under the simple IGM model.

For each parameter, we show plots analogous to Fig. 7 and Fig. 8, as appropriate. From these plots the virial radius and Stromgren radius can be read off, as well as the corresponding IGM infall velocities. The line profile figures show the effect of our model parameters, if any, on the intrinsic line profile, and the effect on the observed line profile.

**Halo mass** In Fig. 9 we recompute the IGM properties for the fiducial model, except that we set the halo mass to  $10^{10}$  or  $10^{12} M_{\odot}$ . Though more massive halos have larger values of  $R_{\text{vir}}$  (the radii at which the curves terminate), they have more negative values of  $v(R_{\text{vir}})$ . More massive halos also have slightly higher IGM densities around them. The combination of larger virial radii (ionizing flux falls off as  $r^{-2}$ ) and slightly higher IGM densities leads to larger neutral fractions within the Stromgren spheres of more massive halos. The Stromgren spheres of more massive halos are slightly smaller (due to larger densities within them), but  $v(R_{\text{S}})$  decreases more dramatically with increasing halo mass.

In Fig. 10 we show the corresponding intrinsic and observed Lyman  $\alpha$  line profiles. More massive halos have broader intrinsic and observed lines (because  $v_{\text{D}} \equiv f_{\text{v}} v_{\text{c}}$  and  $v_{\text{c}}$  increases for more massive halos). A new prediction of the dynamic IGM model is that the offset between the intrinsic line center and the blue edge of the observed line (or, similarly, the centroid of the observed line) increases with increasing halo mass. This conclusion is somewhat dependent on the assumption that the intrinsic Lyman  $\alpha$  emission line is centered on the systemic velocity of the galaxy. In practice



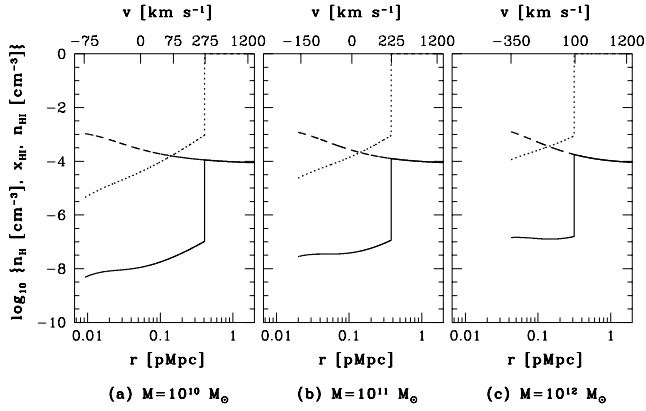


**Figure 9.** As in Fig. 7, but note different radial scale. The curves are truncated at  $R_{\text{vir}}$ . (a) Halo mass  $M = 10^{10} M_{\odot}$ . (b)  $M = 10^{11} M_{\odot}$  (fiducial model). (c)  $M = 10^{12} M_{\odot}$ .

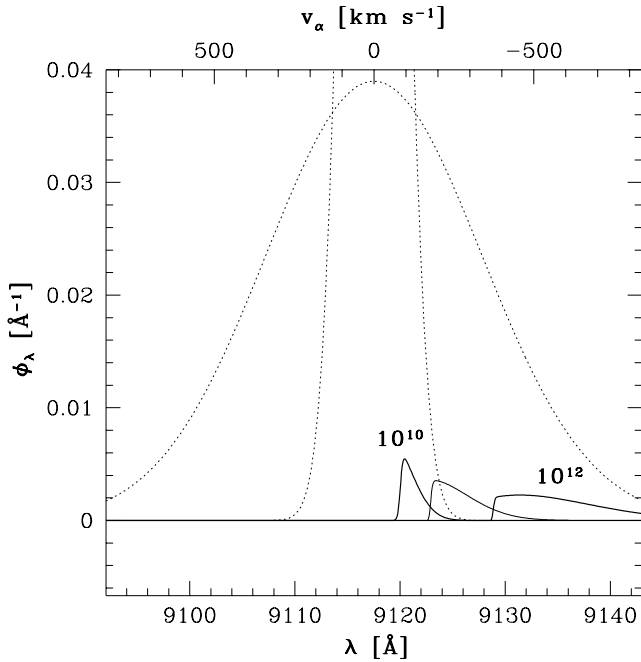


**Figure 10.** As in Fig. 8, but note different axis scales. The labels show  $M$  (in  $M_{\odot}$ ) for the corresponding intrinsic and observed line profiles. The fiducial model  $M = 10^{11} M_{\odot}$  is the lighter curve, and the intrinsic fiducial line profile is not shown.

obtaining the intrinsic Lyman  $\alpha$  line shape may be impossible, but a more complicated model of the intrinsic line may be passed through our IGM model to produce a predicted observed line profile, which will always have a lower limit in wavelength corresponding to  $v_{\alpha} = v(R_{\text{vir}})$ .

**Star-formation rate** In Figs. 11 and 12 we recompute the IGM properties and Lyman  $\alpha$  line profiles for the fiducial model, except that we set the SFR to 1, 100, or  $1000 M_{\odot} \text{ yr}^{-1}$ . Increasing the SFR increases both the size of the Stromgren sphere and the ionization fraction inside. If we decrease the SFR from the fiducial value of  $10 M_{\odot} \text{ yr}^{-1}$  to  $1 M_{\odot} \text{ yr}^{-1}$  then the neutral IGM encroaches all the way to  $v(R_S) = 25 \text{ km s}^{-1}$  (compared to  $v(R_S) = 225 \text{ km s}^{-1}$  in the fiducial case), and thus the damping wing almost com-

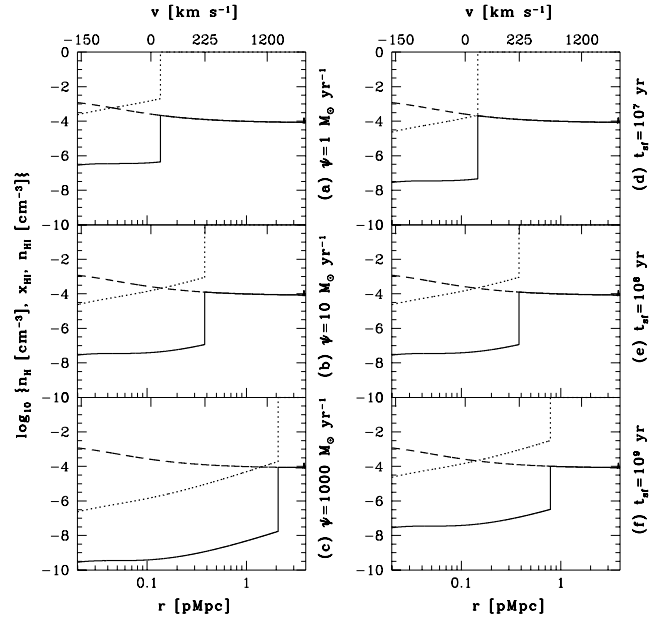


**Figure 11.** As in Fig. 7. (a) Star-formation rate  $\psi = 1 M_{\odot} \text{ yr}^{-1}$ . (b)  $\psi = 10 M_{\odot} \text{ yr}^{-1}$  (fiducial model). (c)  $\psi = 1000 M_{\odot} \text{ yr}^{-1}$ . See Fig. 14c for  $\psi = 10 M_{\odot} \text{ yr}^{-1}$ . (d) Age of star formation  $t_{\text{SF}} = 10^7 \text{ yr}$ . (e)  $t_{\text{SF}} = 10^8 \text{ yr}$  (fiducial model). (f)  $t_{\text{SF}} = 10^9 \text{ yr}$ .

pletely wipes out the observed line. Increasing the SFR to  $100 M_{\odot} \text{ yr}^{-1}$ , the Stromgren sphere expands out to  $v(R_S) = 650 \text{ km s}^{-1}$ . Though there is a decrease in the neutral fraction within the Stromgren sphere, this effect is not sufficient to lift the complete suppression of the observed line at  $v_{\alpha} \gtrsim v(R_{\text{vir}})$ . However, the greater distance (in velocity) to the fully neutral IGM means that the observed line redward of  $v_{\alpha} \simeq v(R_{\text{vir}})$  is less damped than in the fiducial case. A further increase of the SFR to  $1000 M_{\odot} \text{ yr}^{-1}$  expands the Stromgren sphere yet further, resulting in very little damped absorption at  $v_{\alpha} \lesssim v(R_{\text{vir}})$ . Moreover, the neutral fraction inside part of the Stromgren sphere is now small enough that scattering by the cross-section Doppler core no longer completely suppresses the line at  $v_{\alpha} > v(R_{\text{vir}})$ . Note the notch in the spectrum at  $v_{\alpha} = v(R_{\text{vir}})$ ; this is the feature predicted in QSO spectra by Barkana & Loeb (2003a).

**Age of star formation** In Figs. 11 and 13 we recompute the IGM and line profile properties for the fiducial model, except that we set the age of star formation to  $10^7$  or  $10^9 \text{ yr}$ . Changing  $t_{\text{SF}}$  changes the size of the Stromgren sphere, but does not change the ionization balance within it. Thus the effect on the observed line profile is only to change the amount of damping of the line at  $v_{\alpha} < v(R_{\text{vir}})$ .

**Escape fraction of ionizing photons** In Fig. 14 we recompute the IGM properties for the fiducial model, except that we set  $f_{\text{esc}} = 0$  or 1. Scaling  $f_{\text{esc}}$  has the same effect as scaling the star-formation rate by the same factor, so the fiducial model modified to  $f_{\text{esc}} = 1$  is the same as the fiducial model modified to  $\psi = 100 M_{\odot} \text{ yr}^{-1}$  (see above). In the case of vanishing escape fraction, for any reasonable value of the SFR the line will unobservable, because a neutral IGM down to  $v(R_{\text{vir}})$  allows only  $4 \times 10^{-5}$  of the intrinsic line to be observed. See also Section 6.2.

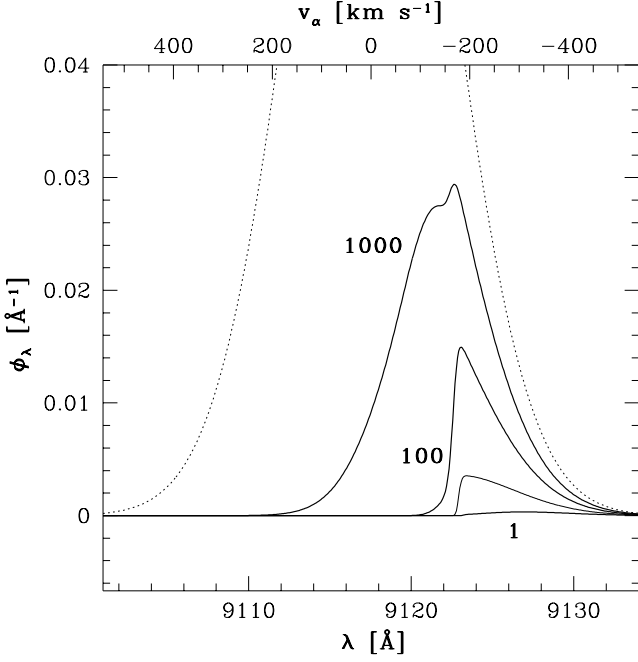


**Figure 12.** As in Fig. 8, but different vertical scale. The labels show star-formation rate (in  $\text{M}_\odot \text{yr}^{-1}$ ) for the corresponding observed line profiles. The fiducial model  $\psi = 10 \text{ M}_\odot \text{yr}^{-1}$  is the lighter curve, and the intrinsic fiducial line profile is the dotted curve.

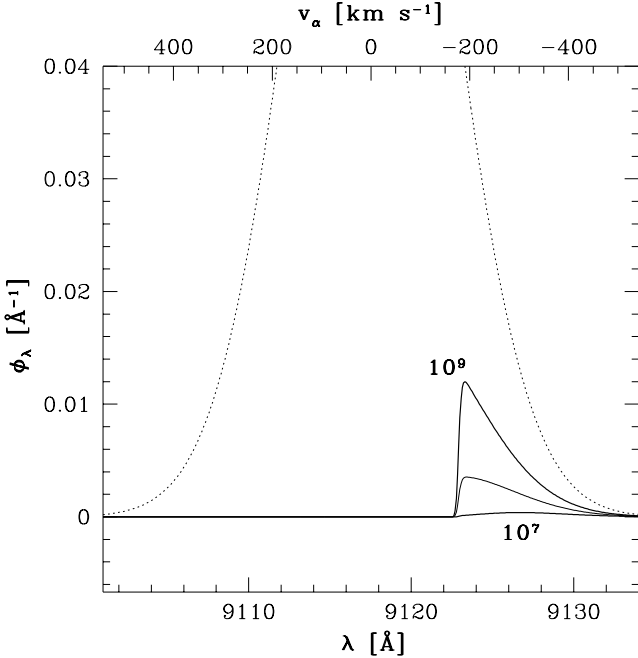


**Figure 13.** As in Fig. 8, but different vertical scale. The labels show the age of star-formation (in yr) for the corresponding observed line profiles. The fiducial model  $t_{\text{SF}} = 10^8 \text{ yr}$  is the lighter curve, and the intrinsic fiducial line profile is the dotted curve.

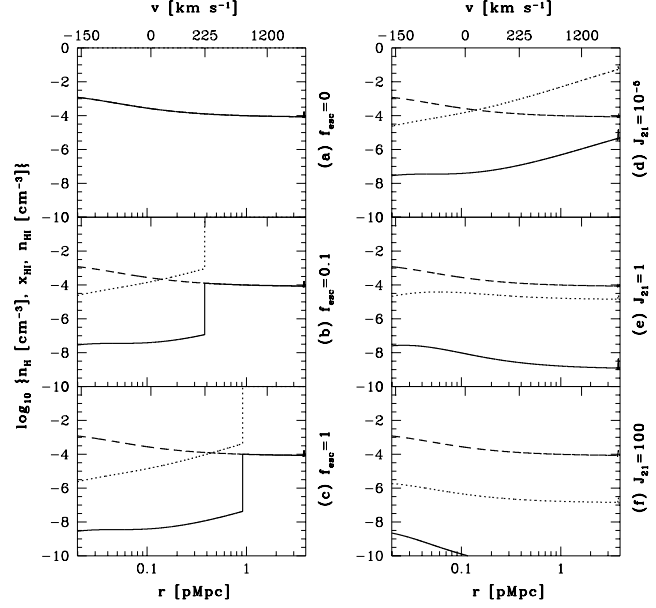


**Figure 14.** As in Fig. 7. (a) Ionizing photon escape fraction  $f_{\text{esc}} = 0$ . (b)  $f_{\text{esc}} = 0.1$  (fiducial model). (c)  $f_{\text{esc}} = 1$ . (d) Ionizing background  $J_{21} = 10^{-5}$ . (e)  $J_{21} = 1$ . (f)  $J_{21} = 100$ .

**Velocity width factor** In Fig. 15 we recompute line profile properties for the fiducial model, except that we set  $f_v = 1$  or 2 ( $f_v$  does not influence the IGM properties). Larger values of  $f_v$  broaden the line, resulting in a greater observable fraction of the intrinsic line. In the limit of much larger values of  $f_v$ , more of the line would be transmitted, but the line width would be so large that spectroscopic detection of the line would become more difficult than for a narrower line with less flux. However, for the values of  $f_v$  we consider, which should bound the actual values, the observed line is still relatively narrow and larger values of  $f_v$  produce more easily observed lines.

#### 4.4 IGM ionization dependence

In this section we vary the ionization state of the IGM to show how this influences the observed Lyman  $\alpha$  line. First we will assume, in contrast to the IGM models considered so far, that there is a mean ionizing background in the IGM that contributes to the ionization of the IGM around the halo, in addition to the contribution from the galaxy itself. We assume that the universe was reionized before star formation turned on in the halo (that is, reionization occurred longer than  $t_{\text{SF}}$  ago), and since then the background has been fixed at

$$J_{21} \equiv \frac{J_\nu}{10^{-21} \text{ erg s}^{-1} \text{ cm}^{-2} \text{ Hz}^{-1} \text{ sr}^{-1}}. \quad (21)$$

For the fiducial values of  $z = 6.5$  and  $t_{\text{SF}} = 10^8 \text{ yr}$ , that corresponds to reionization before  $z = 7.2$ .

In Figs. 14 and 16 we show the properties of the IGM and Lyman  $\alpha$  line profiles for values of the ionizing background that bracket the physically interesting regimes. First we discuss  $J_{21} = 10^{-5}$ , a value so small that the IGM ionization state inside the galaxy's light sphere is completely dominated by the galaxy's ionizing radiation. The light sphere

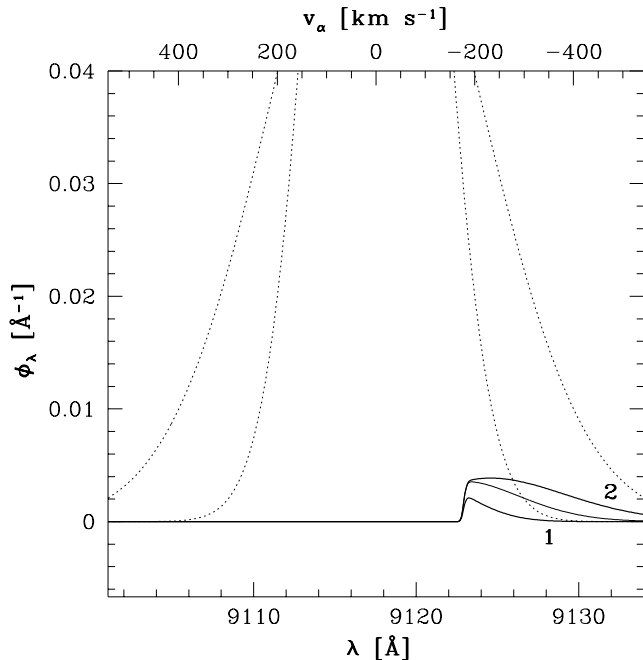


**Figure 15.** As in Fig. 8, but different vertical scale. The labels show the conversion factor  $f_v$  between Doppler line width and halo circular velocity for the corresponding intrinsic and observed line profiles. The fiducial model  $f_v = 1.5$  is the lighter curve, and the intrinsic fiducial line profile is not shown.

has a radius of  $ct_{\text{SF}} = 31$  pMpc for  $t_{\text{SF}} = 10^8$  yr, corresponding to an IGM velocity of almost  $2.5 \times 10^4$  km s $^{-1}$ . Consequently, the IGM ionization state outside of the light sphere is irrelevant.

Even though the ionizing background does not contribute at all to the ionization rate (see eq. 13) at any radius of interest, the pre-reionization of the universe before the galaxy turned on allows its Stromgren sphere to expand at near light speed. Consequently even the IGM at the velocity of 1200 km s $^{-1}$  has a neutral fraction of 0.01. By the Gunn-Peterson trough test, this IGM wouldn't even qualify as reionized. However, this level of ionization completely eliminates any damping wing optical depth. Thus the observed line profile follows the intrinsic line profile from the red wing up to  $v_\alpha = v(R_{\text{vir}})$ , then goes to zero as in the fiducial case. This is the observed behavior for any ionizing background with  $J_{21} \lesssim 1$ , the range observed at  $z < 5$  (Scott et al. 2000).

Ionizing backgrounds in the range  $J_{21} \sim 10$ –100 strongly ionize the mean density IGM. Since the IGM density decreases from a local maximum at  $R_{\text{vir}}$  toward the cosmic mean as a function of increasing radius, IGM gas just outside of the virial radius still strongly scatters the intrinsic line at  $v_\alpha$  corresponding to the velocity of the overdense gas. As the density decreases, though, the neutral fraction drops as well, and the combination leads to greater transmission of the intrinsic line *toward the blue side of the line*. This would generate an unusually-shaped observed line with two peaks, one of which lies to the blue of the intrinsic line center.

At yet higher values of  $J_{21} \gtrsim 10^3$ , the IGM is so strongly ionized that the entire intrinsic line would be observed. We note again that we expect  $J_{21} \lesssim 1$ , though we are unaware

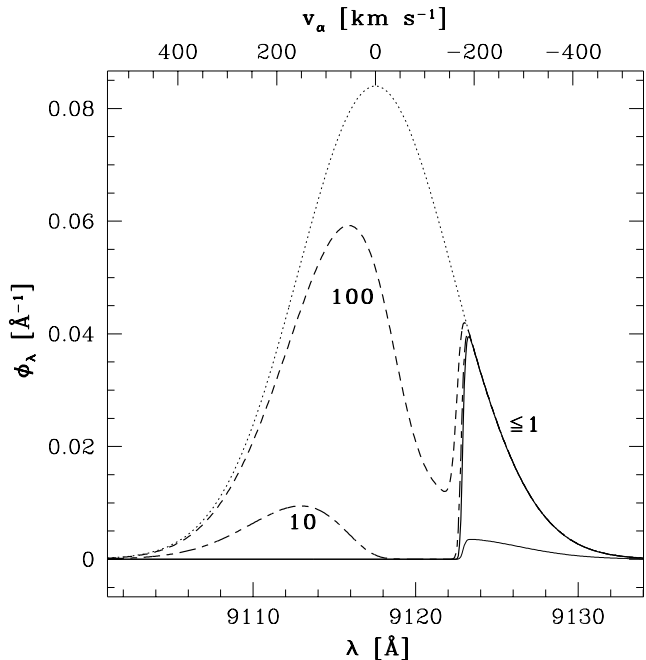


**Figure 16.** As in Fig. 8. The labels show ionizing background strength  $J_{21}$  for the corresponding observed line profiles. The fiducial model with no ionizing background is the lighter curve, and the intrinsic fiducial line profile is the dotted curve.

of any predictions for  $J_{21}$  at  $z > 6$  in models that reproduce the *WMAP* optical depth value.

Alternately, rather than considering a fixed ionizing background in a reionized universe, we can fix the neutral fraction of the IGM outside of the galaxy's Stromgren sphere,  $x_{\text{HI}}^{\text{IGM}}$ . This approach is more useful for considering a weakly-ionized IGM with  $x_{\text{HI}}^{\text{IGM}} \sim 0.5$  (e.g., Cen 2003a, where a fully reionized universe almost entirely recombinates). Figure 17 shows the observed Lyman  $\alpha$  line profiles of the fiducial galaxy when  $x_{\text{HI}}^{\text{IGM}}$  is set to 0.5 and 0.05. As expected, the decreased H I abundance in the ‘neutral’ IGM means that the red wing of the Lyman  $\alpha$  line is less suppressed by damping wing scattering. There is no effect on the Doppler scattering that scatters the center of the intrinsic line. See also Section 6.2.

#### 4.5 Redshift dependence

Last, we turn to the effects due solely to changes in redshift. In the future there will (hopefully) be surveys for strong Lyman  $\alpha$  emission lines at several different redshifts at  $z > 6$ . We study redshift dependence by keeping the other free parameters fixed; realistically, other parameters, such as star-formation rate, age of star formation, escape fraction, and the typical halo mass, may also depend on redshift. Comparison of the galaxy/halo parameter dependencies described above in conjunction with the effects shown here can be used to predict trends for a specific model of the evolution of the galaxy/halo parameters. Disentangling the redshift dependence of the IGM ionization state from the other redshift dependences may still be very difficult in practice.

Proceeding with simple cases to understand the expected effects, we place the fiducial halo at  $z = 8.8$  and

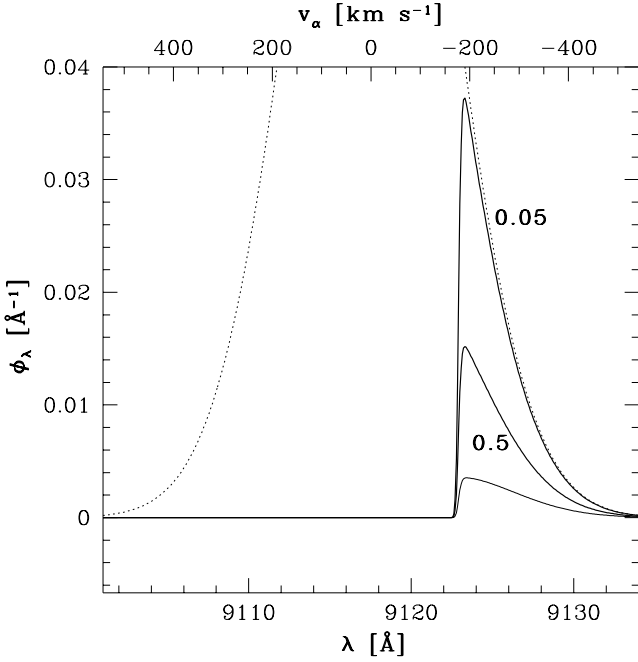


**Figure 17.** As in Fig. 8, but with different vertical scale. The labels show the neutral fraction of the IGM outside of the galaxy's Stromgren sphere for the corresponding observed line profiles. The fiducial model with a neutral IGM is the lighter curve, and the intrinsic fiducial line profile is the dotted curve.

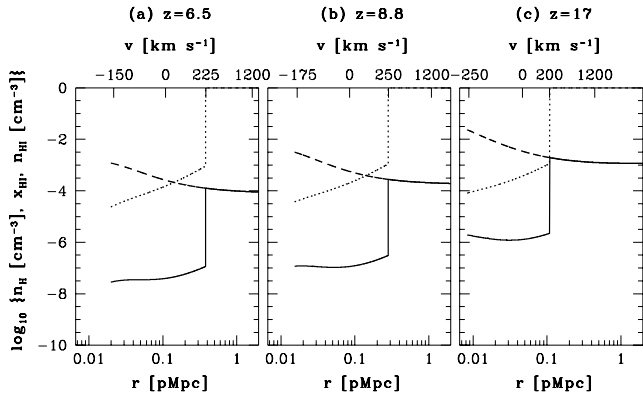


**Figure 18.** As in Fig. 7, but note different radial and velocity scales. The curves are truncated at  $R_{\text{vir}}$ . (a) Redshift  $z = 6.5$  (fiducial model). (b)  $z = 8.8$ . (c)  $z = 17$ .

$z = 17$ . Figures 18 and 19 show the IGM and Lyman  $\alpha$  line profile properties. Because we keep the mass of the halo fixed, the virial radius shrinks at increasing redshift. This results in an increasingly negative velocity of the IGM at the virial radius. The IGM is also denser at higher redshift, resulting in higher neutral fractions when the ionization balance is calculated. An additional effect is the increased circular velocity of the halo, which broadens the intrinsic line.

## 5 GALACTIC WINDS

We now consider another, possibly crucial, alteration to the model of Lyman  $\alpha$  emitter plus IGM scattering described so

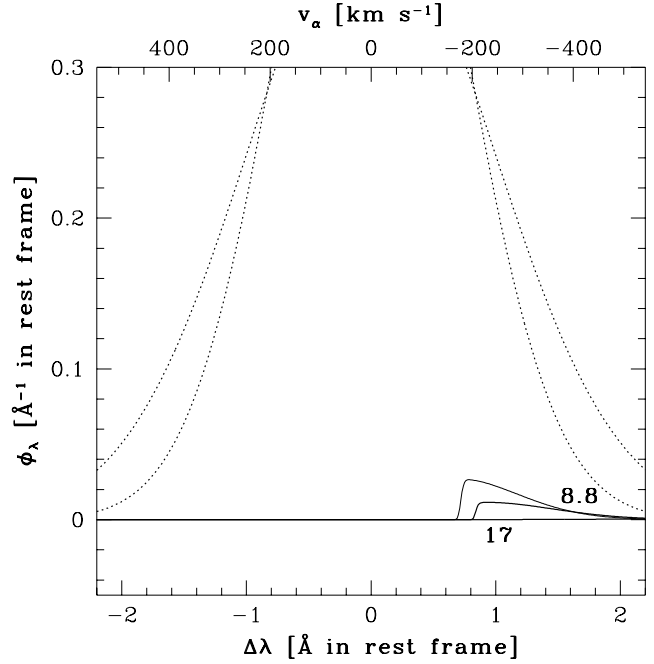


**Figure 19.** Lyman  $\alpha$  line profiles. The wavelength scale is expressed as an offset from the Lyman  $\alpha$  resonance in the frame of the galaxy, chosen so that the  $v_\alpha$  scale is the same as in Fig. 8. The labels show the redshift for the corresponding observed line profiles. The narrower intrinsic profile (dotted curve) is for  $z = 8.8$ ; the wider intrinsic profile (dotted curve) is for  $z = 17$ . The fiducial model  $z = 6.5$  is the lighter curve, and the intrinsic fiducial line profile is not shown.

far. High velocity ( $\sim 360 \text{ km s}^{-1}$ ) redshifts of Lyman  $\alpha$  emission compared to other interstellar features are observed in  $z = 3$  Lyman Break Galaxies (Shapley et al. 2003); QSO absorption line cross-correlation suggests that these winds may have blown to large distances ( $\sim 0.2 \text{ pMpc}$ , Adelberger et al. 2003).

Galactic winds, if present in galaxies at  $z > 6$ , may have two important consequences for the interpretations of Lyman  $\alpha$  emission from galaxies during reionization. The first is that as the wind blows through the IGM, it may collisionally ionize the hydrogen it passes, increasing the ionization fraction of this gas (Adelberger et al. 2003). The second effect is that the intrinsic Lyman  $\alpha$  line may not have a Doppler shape centered on the galaxy's redshift. Instead, it may already display an asymmetric profile centered considerably to the red of the systemic redshift (Shapley et al. 2003, where they find a mean redshift of  $360 \text{ km s}^{-1}$ ). Inspection of Fig. 6 shows that the IGM optical depth for the fiducial galaxy is only  $\sim 1$  at redshifts of more than  $200 \text{ km s}^{-1}$ .

Since we lack a good physical model to calculate wind properties, we adopt a very simple assumption to illustrate the possible effects of large-scale winds on the IGM (the first effect described above). We assume that a wind blows out to

<sup>4</sup> Note that in observations velocity (and redshift) is measured in the observer's frame, whereas in our plots  $v_\alpha$  is in the frame of the emitting galaxy, hence a line redshifted by  $360 \text{ km s}^{-1}$  falls at  $v_\alpha = -360 \text{ km s}^{-1}$ .

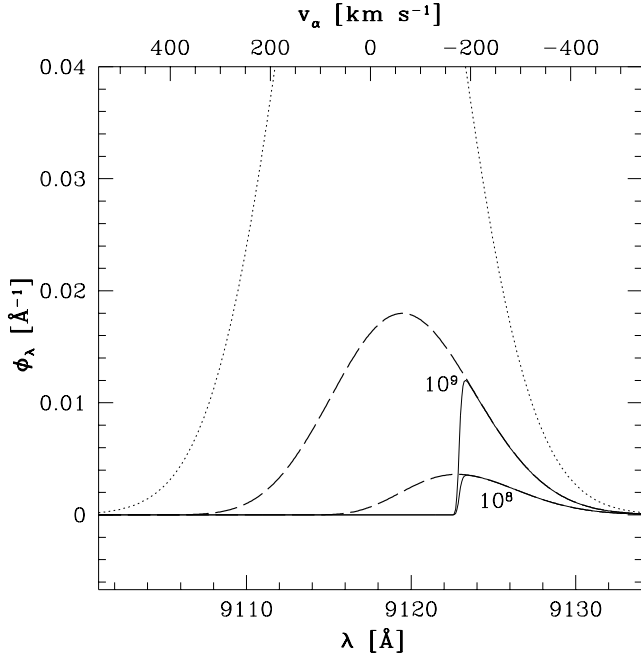


**Figure 20.** As in Fig. 8, but different vertical scale. The labels show star-formation timescale (in yr) for the corresponding observed line profiles. For each  $t_{\text{SF}}$ , the light solid curve is the profile without assuming any winds (as in Fig. 13), and the long-dashed curve is the observed line profile assuming a wind blows to the Stromgren radius. The intrinsic fiducial line profile is the dotted curve.

the Stromgren radius of the galaxy (see Fig. 11), completely ionizing all of the gas within that radius. Figure 20 shows the observed Lyman  $\alpha$  line profiles including such winds. The result for the fiducial model is that the observed line becomes roughly symmetric, though still centered to the red of the intrinsic line center, and the observed flux doubles. If  $t_{\text{SF}}$  is changed to  $10^9$  yr, the Stromgren sphere is much larger (see Fig. 11) and the observed flux increases by almost a factor of 5.

The required wind velocity can be calculated by dividing the Stromgren radii (illustrated in previous plots) by  $t_{\text{SF}}$ . For the fiducial halo, the Stromgren radius is 0.38 pMpc, giving a wind velocity over  $10^8$  yr of  $3700 \text{ km s}^{-1}$ . Almost any wind model would predict a smaller wind velocity than this, so though Fig. 20 shows the qualitative effect, even the  $10^8$  yr curve is an overestimate of the true effect, assuming galactic winds blow to 0.2 pMpc, as in Adelberger et al. (2003).

Winds don't affect the damping wing suppression of the line from absorption by neutral (in the case of a non-reionized IGM) gas outside of the Stromgren sphere (the solid and long-dashed curves match at  $v_\alpha < v(R_{\text{vir}})$ ). Thus the depression of the observed line profiles compared to the intrinsic line profiles of plots like Fig. 8 can be used to estimate the transmission of a highly-redshifted Lyman  $\alpha$  line. Since the damping wing optical depth is set by the IGM outside of the Stromgren sphere, parameters that affect the size of the Stromgren sphere (e.g.,  $t_{\text{SF}}$ , Fig. 11), and the ionization state of the IGM (e.g.,  $J_{21}$ , Fig. 14, and  $x_{\text{HI}}^{\text{IGM}}$ ), have a large influence on the transmission at  $v_\alpha < v(R_{\text{vir}})$ . In the next section we illustrate the effect galactic winds may

have on the observed Lyman  $\alpha$  line for all of the parameter variations discussed in Section 4.

## 6 DISCUSSION

### 6.1 Lyman $\alpha$ line fluxes

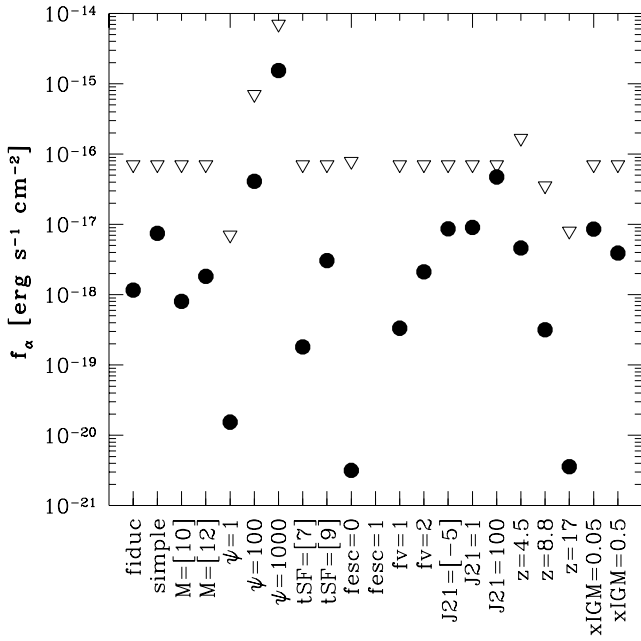
First we present three plots to summarize the results of the previous sections. Figure 21 shows the intrinsic Lyman  $\alpha$  line flux (calculated as described in Section 3.1) as open triangles for each model listed on the bottom axis. The solid circles show the integrated flux of the observed Lyman  $\alpha$  line calculated from the intrinsic Lyman  $\alpha$  line flux and observed line profiles presented in Section 4.

Figure 22 shows the intrinsic Lyman  $\alpha$  line flux as open triangles for each model, as in Fig. 21. Here the open squares are the integrated flux of the observed Lyman  $\alpha$  line calculated assuming a galactic wind completely ionizes the IGM out to the Stromgren radius of the galaxy (see Section 5; this is probably an overestimate of the expected effect, but comparison with Fig. 21 shows that for many models this is a small effect regardless). The solid diamonds are the integrated flux of the observed Lyman  $\alpha$  line calculated assuming the intrinsic Lyman  $\alpha$  line is emitted entirely at  $360 \text{ km s}^{-1}$  redward of the systemic Lyman  $\alpha$  wavelength (see Section 5). The consequence of moving the intrinsic line to the red is that the observed line flux is generally at least 20 per cent of the intrinsic line flux for most of the models (independent of whether or not the wind blows into the IGM). This is illustrated more explicitly in Figure 23. However, more massive galaxies with  $v(R_{\text{vir}}) \lesssim 360 \text{ km s}^{-1}$  (such as our  $M = 10^{12} M_\odot$  model) would require Lyman  $\alpha$  lines even more redshifted than  $360 \text{ km s}^{-1}$  to make a difference compared to the no-wind model. There is no solid diamond for  $M = 10^{12} M_\odot$  in either Fig. 22 or Fig. 23 because the IGM transmission at  $v_\alpha = -360 \text{ km s}^{-1}$  is formally zero. A realistic line profile (not concentrated entirely at  $v_\alpha = -360 \text{ km s}^{-1}$ ) would result in a flux similar to the no-wind model.

Figure 23 shows the transmission of the Lyman  $\alpha$  line,  $T_\alpha$ , defined as the ratio of the observed to intrinsic Lyman  $\alpha$  line flux. The shapes of the symbols match their shapes in Figs. 21 and 22. Quite generally, an intrinsic Lyman  $\alpha$  line redshifted by  $360 \text{ km s}^{-1}$  produces an observed line suppressed by less than a factor of 5, for galaxies at  $z = 6.5$  in a neutral IGM. If the IGM is reasonably ionized, a redshifted Lyman  $\alpha$  line may survive almost unscattered (e.g., solid diamond for  $x_{\text{HI}}^{\text{IGM}} = 0.05$  model), whereas if the intrinsic line is at the systemic redshift in those models, the observed line is almost an order of magnitude weaker (e.g., open circle for  $x_{\text{HI}}^{\text{IGM}} = 0.05$  model).

### 6.2 Observed $z = 6.5$ Lyman $\alpha$ emitters

To compare observed Lyman  $\alpha$  line fluxes to our predictions, we need an estimate of the intrinsic line flux. The observed Lyman  $\alpha$  line flux provides a lower limit to the intrinsic flux, but current observations of  $z = 6.5$  do provide one avenue to estimate the intrinsic flux. The UV continuum to the red of the Lyman  $\alpha$  is a star-formation rate indicator (Kennicutt 1998); near-IR photometry of  $z = 6.5$  galaxies provides an



**Figure 21.** Intrinsic and observed Lyman  $\alpha$  line flux as a function of model parameters. Each model plotted is described by a label on the bottom axis that refers to the fiducial model in the case of ‘fiduc,’ and refers to the parameter varied from the fiducial model in the rest of the cases (see Section 4). Numbers in square braces are the  $\log_{10}$  of the parameter value. The open triangles are the intrinsic Lyman  $\alpha$  line flux, and the solid circles are the observed Lyman  $\alpha$  line flux, based on the line profiles calculated in Section 4.

estimate of their rest-frame UV continua. Two of the three confirmed  $z = 6.5$  galaxies have SFRs estimated in this way:  $10 \text{ M}_{\odot} \text{ yr}^{-1}$  for HCM 6A (hereafter ‘H,’ Hu et al. 2002b), and  $36 \text{ M}_{\odot} \text{ yr}^{-1}$  for SDF J132415.7+273058 (hereafter ‘K,’ Kodaira et al. 2003) (in our cosmology). As discussed in Section 3.1, converting the SFR to an intrinsic Lyman  $\alpha$  line flux depends on many parameters, but for our fiducial choices we estimate intrinsic Lyman  $\alpha$  line luminosities of  $3.4 \times 10^{43} \text{ erg s}^{-1}$  for H and  $1.2 \times 10^{44} \text{ erg s}^{-1}$  for K. Note that both Hu et al. (2002a) and Kodaira et al. (2003) estimate Lyman  $\alpha$  lower intrinsic luminosities by using an empirical relation between H $\alpha$  luminosity and SFR (Kennicutt 1998) and converting H $\alpha$  luminosity to Lyman  $\alpha$  luminosity. The corresponding intrinsic Lyman  $\alpha$  line fluxes are  $6.9 \times 10^{-17} \text{ erg s}^{-1} \text{ cm}^{-2}$  for H and  $2.4 \times 10^{-16} \text{ erg s}^{-1} \text{ cm}^{-2}$  for K. Comparison with the observed Lyman  $\alpha$  fluxes (corrected for lensing in the case of ‘H’) gives estimated observed to intrinsic ratios of  $T_{\alpha} = 0.09$  for both H and K.

From Fig. 23 we see that appropriate models with a neutral IGM and some velocity offset between the intrinsic Lyman  $\alpha$  line and the systemic galaxy redshift can produce values of  $T_{\alpha} \sim 0.1$ . Alternately models with a partially or mostly ionized IGM without any wind effect also have  $T_{\alpha} \sim 0.1$ .

The redshift of the intrinsic Lyman  $\alpha$  line with respect to the systemic redshift of the galaxy is a clearly key parameter for interpreting observed Lyman  $\alpha$  lines. Fortunately it may be estimated from non-resonant recombination lines, such as H $\alpha$  or H $\beta$ . For galaxies at  $z \gtrsim 6.5$  these lines fall at  $\lambda \gtrsim 3.6 \text{ } \mu\text{m}$ , unobservable from the ground in the near-

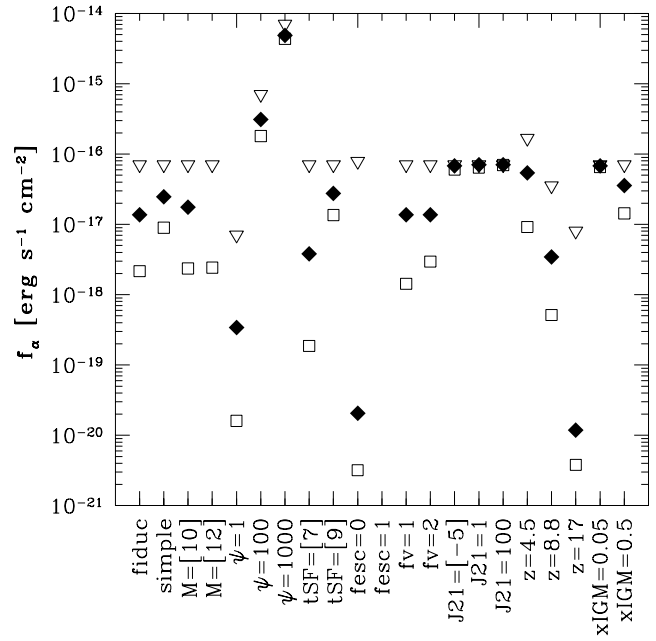


**Figure 22.** Intrinsic and observed Lyman  $\alpha$  line flux as a function of model parameters, including possible effects due to galactic winds. The model labelling is described in Fig. 21. The open triangles are the intrinsic Lyman  $\alpha$  line flux, as in Fig. 21. The open squares are the integrated flux of the observed Lyman  $\alpha$  line calculated assuming a galactic wind completely ionizes the IGM out to the Stromgren radius of the galaxy. The solid diamonds are the integrated flux of the observed Lyman  $\alpha$  line calculated assuming the intrinsic Lyman  $\alpha$  line is emitted entirely at  $360 \text{ km s}^{-1}$  redward of the systemic Lyman  $\alpha$  wavelength. See Section 5.

future. The *James Webb Space Telescope (JWST)* is projected to have sufficient sensitivity to detect H $\alpha$  and H $\beta$  from the  $z = 6.5$  galaxies discovered so far. Measurements of H $\alpha$  and H $\beta$  will also provide another SFR estimate (with  $f_{\text{esc}}$  no longer entering into the conversion between SFR and intrinsic Lyman  $\alpha$  line flux), as well as a dust extinction estimate.

An example of an optimistic future observation would be a measurement of H $\alpha$  and H $\beta$  line redshifts and fluxes for a  $z = 6.5$  galaxy with a measured Lyman  $\alpha$  line and UV continuum. If the ratio of H $\alpha$  to H $\beta$  line flux matches the prediction for no extinction, and the SFR deduced from from those Balmer lines agrees with the SFR estimated from the UV continuum, then a reasonable conclusion would be that dust extinction is not very important in the galaxy<sup>5</sup>. Proceeding under the assumption of a normal IMF and no extinction, the intrinsic Lyman  $\alpha$  line flux may then be estimated. If the Lyman  $\alpha$  line were found to be centered near the Balmer line redshift (assumed to be the systemic redshift of the galaxy), then we could compare the measured value of  $T_{\alpha}$  with the circles in Fig. 23; at that point a  $T_{\alpha}$  could be converted into an estimate of the neutral fraction of the IGM, though with plenty of uncertainty associated with unknown parameters such as  $M$ ,  $t_{\text{SF}}$ , and  $f_v$ . A more clear-cut

<sup>5</sup> This conclusion could be strengthened by a stringent upper limit on, e.g., He II 1640 Å, a line that would be present for an IMF weighted toward very massive stars, (Schaerer 2003).

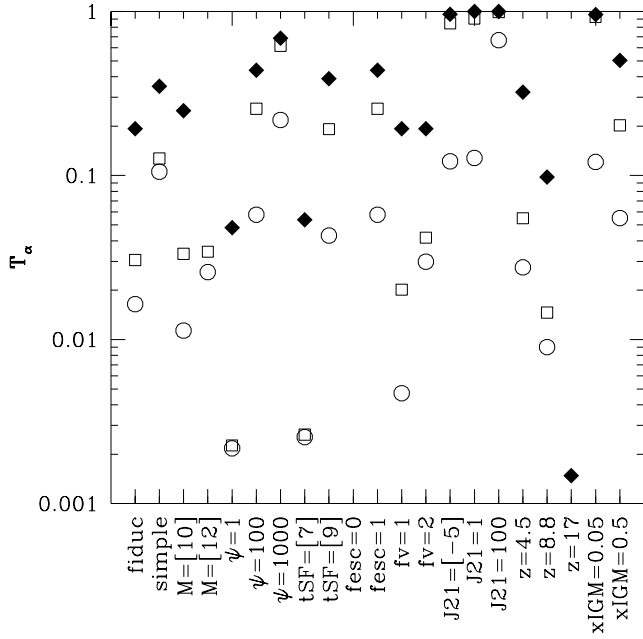


**Figure 23.** Ratio of observed to intrinsic Lyman  $\alpha$  line flux as a function of model parameters, for both no wind and wind models. The model labelling is described in Fig. 21. The point shapes are the same as in Figs. 21 and 22: open circles show no-wind models, open squares show models where a strong wind clears the Stromgren sphere of IGM, and solid diamonds show models where the intrinsic Lyman  $\alpha$  is concentrated at  $360 \text{ km s}^{-1}$  redward of the systemic redshift.

conclusion may be reached if the Lyman  $\alpha$  line is found to be substantially redshifted compared to the Balmer redshift and the measured  $T_\alpha$  is close to 1. This would be a strong signal that the IGM was mostly ionized at that redshift (see below), and may moreover place an interesting limit on the mass of the halo, depending on the shape of the observed Lyman  $\alpha$  line.

In advance of *JWST*, Fig. 23 makes it clear that drawing any firm conclusions regarding the ionization fraction of the IGM based only on the observed Lyman  $\alpha$  lines and UV continua of  $z = 6.5$  is very difficult.

Before moving on, we present two more plots of interest regarding the observability of Lyman  $\alpha$  lines. We have seen that large Stromgren spheres around galaxies allow more of the intrinsic Lyman  $\alpha$  line to be observed (e.g., Fig. 13). The ionization of the IGM is directly proportional to the parameter  $f_{\text{esc}}$ , so the largest possible Stromgren sphere is created when  $f_{\text{esc}} = 1$ . However, since the intrinsic Lyman  $\alpha$  line flux is proportional to  $(1 - f_{\text{esc}})$ , the strongest intrinsic Lyman  $\alpha$  line is produced when  $f_{\text{esc}} = 0$ . Clearly the strongest *observed* line comes from some intermediate value of  $f_{\text{esc}}$ . In Fig. 24 we plot the intrinsic and observed Lyman  $\alpha$  line flux for two models, the fiducial model, and the  $\psi = 100 \text{ M}_\odot \text{ yr}^{-1}$  model. The observed line flux in both models peaks near  $f_{\text{esc}} = 0.35$ .

Once reliable estimates of  $T_\alpha$  are available, they can be used to estimate the neutral fraction of the IGM in the interesting regime of  $x_{\text{HI}} \sim 0.5$ . Figure 25 illustrates  $T_\alpha$  as a function of the model parameter  $x_{\text{HI}}^{\text{IGM}}$  (see Section 4.4), for the fiducial galaxy. The solid curve was calculated assum-

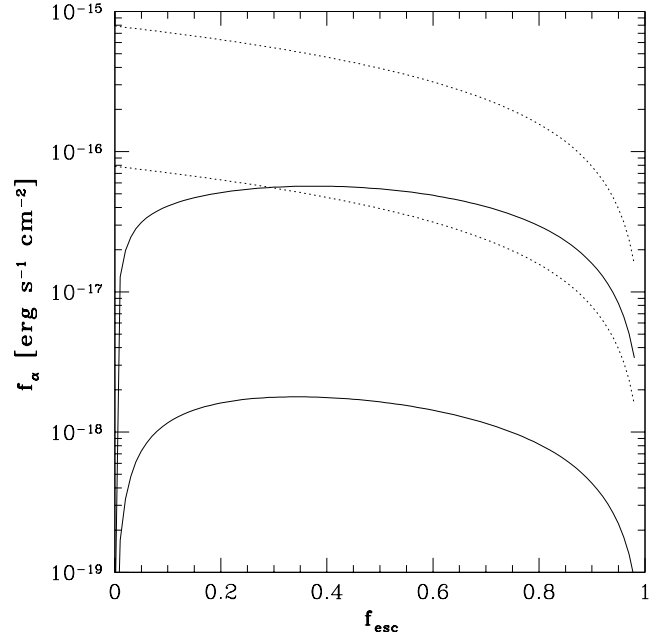


**Figure 24.** Intrinsic and observed Lyman  $\alpha$  line flux as a function of ionizing photon escape fraction. The dotted curves are the intrinsic Lyman  $\alpha$  line flux; the solid curves are the observed line fluxes. The lower curves are for the fiducial model with  $f_{\text{esc}}$  varied; the upper curves are for the fiducial model modified to  $\psi = 100 \text{ M}_\odot \text{ yr}^{-1}$ .

ing a Doppler profile intrinsic Lyman  $\alpha$  line centered at the galaxy's systemic redshift, and the long-dashed curve was calculated assuming the intrinsic Lyman  $\alpha$  line is concentrated  $360 \text{ km s}^{-1}$  redward of the systemic velocity. While an accurate measurement of  $T_\alpha$  can constrain the IGM neutral fraction, this is only possible with reasonable knowledge of the redshift of the intrinsic Lyman  $\alpha$  line compared to the systemic velocity of the galaxy.

### 6.3 Model assumptions

Now we return to a discussion of the assumptions made in this paper and their possible consequences on our conclusions. First we discuss the possible effects of dust in a Lyman  $\alpha$  emitting galaxy. If dust absorbs ionizing photons, then the star-formation rate in our models can simply be rescaled to take that into account. Alternately, dust may extinct the Lyman  $\alpha$  line and UV continuum almost equally, but extinct the Balmer lines considerably less. In this case the Lyman  $\alpha$  line extinction can be estimated and corrected for. Dust may also affect the UV continuum differently from the recombination emission, in the event that dust is distributed differently with respect to stars and H II regions. In this case the extinction value measured by the Balmer lines alone (with an extinction curve) may be used to correct the Lyman  $\alpha$  line, assuming that resonant photons are extincted no differently than non-resonant photons.

Dust extinction can cause great ambiguity in the interpretation of Lyman  $\alpha$  lines, even when UV continuum and Balmer lines are measured, because resonant Lyman  $\alpha$  photons may be extincted differently from non-resonant UV continuum and Balmer line photons. Dust may extinct Lyman  $\alpha$

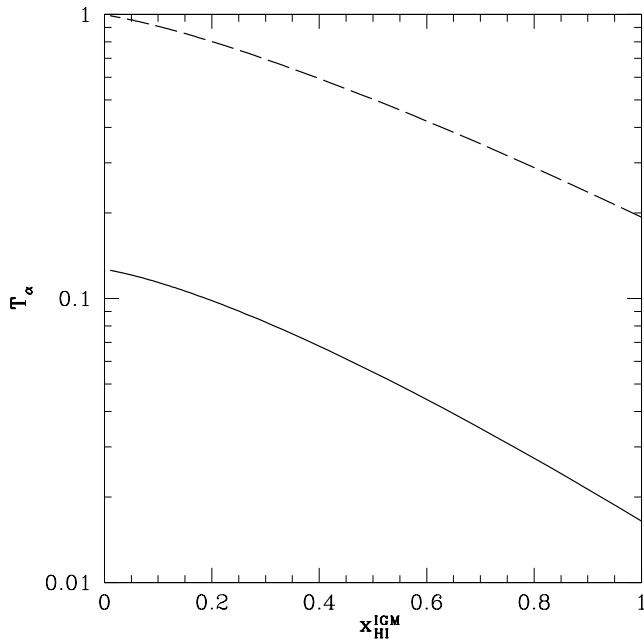


**Figure 25.** Ratio of observed to intrinsic Lyman  $\alpha$  line flux as a function of  $x_{\text{HI}}^{\text{IGM}}$ . The solid curve assumes the intrinsic line profile described in Section 3.1. The long-dashed curve assumes the intrinsic Lyman  $\alpha$  line is concentrated  $360 \text{ km s}^{-1}$  redward of the systemic velocity (see Section 5). Both curves are for the fiducial galaxy.

photons preferentially over UV continuum photons, due to the extra path-length through the galaxy that resonantly scattered photons travel before escaping. Certain gas and dust geometries, however, may mitigate or even reverse that effect (Neufeld 1991). There is no direct observable to measure this possible effect, except that an extinction-corrected SFR estimated from Balmer lines does place an upper limit on the intrinsic Lyman  $\alpha$  line flux.

More fundamental assumptions are associated with our model of the IGM around Lyman  $\alpha$  emitting galaxies. We assumed the presence of an accretion shock at the virial radius of the halo containing the galaxy (see also Barkana & Loeb 2003b). If these galaxies have no accretion shock, as suggested by Birnboim & Dekel (2003), then our conclusions are greatly changed. It is the presence of the accretion shock that generates the characteristic wavelength scale where line transmission begins (see Section 4.2). In the absence of a virial shock, the infalling gas will eventually shock when it reaches the galaxy. The observed Lyman  $\alpha$  line would be suppressed blueward of that velocity, implying only intrinsic Lyman  $\alpha$  lines that were very redshifted with respect to the systemic redshift of the galaxy could be observed. Another consequence of the lack of a virial shock is that Lyman  $\alpha$  emission from the cooling of the IGM gas would be located close to the galaxy (Birnboim & Dekel 2003), thus any observed Lyman  $\alpha$  line may have a contribution from contribution from cooling radiation as well as star-formation powered Lyman  $\alpha$ . If future observations show an extremely redshifted Lyman  $\alpha$  lines at high redshifts, this may be indicative of cooling radiation from IGM gas falling unshocked down to the center of a halo.

In Section 3.2.1 we discussed our assumptions about

the density distribution of the IGM around the Lyman  $\alpha$  emitting galaxy. We calculate the ensemble-averaged IGM density distribution; even for the spherically-averaged density profile, deviations from this average are expected from galaxy to galaxy. Additionally, we estimated that structure near the emitting galaxy has only a small effect on the density distribution of the IGM. However, we did not address the effect of collapsed and collapsing structures on the velocity field of the IGM, which is crucial (more so than IGM density) to our predicted line profiles. Numerical simulations may be used to estimate both the variance in the IGM structure from galaxy to galaxy, and also the density and velocity distributions of the IGM along the line of sight toward a galaxy accounting for substructure.

## 7 SUMMARY

We have calculated observed Lyman  $\alpha$  line profiles for high-redshift galaxies, with a focus on the prospects of using observed Lyman  $\alpha$  lines to probe the ionization of the universe at  $z > 6.5$ . Toward this end we have investigated many of the parameters that influence the observed Lyman  $\alpha$  line from a high-redshift galaxy. We conclude that future measurements with *JWST* may permit the estimation of IGM neutral fractions at  $z > 6.5$ , but current  $z = 6.5$  data do not yet place a strong constraint on the neutral fraction at that redshift if we allow consideration of galactic winds. If we take at face value our estimates of the integrated Lyman  $\alpha$  transmission of the two  $z = 6.5$  galaxies for which estimation is possible, and assume our simplest model (with no winds), we would conclude that the IGM neutral fraction is  $x_{\text{HI}} \lesssim 0.1$  at  $z = 6.5$ .

Interpretation of an observed Lyman  $\alpha$  line alone (or even with a measurement of the UV continuum) is extremely difficult, due to the host of parameters that influence it. However there is hope that with the rest-frame optical spectra that *JWST* will provide for high-redshift galaxies, Lyman  $\alpha$  emission lines will yet prove fruitful for constraining the reionization history of the universe at  $z > 6.5$ .

## ACKNOWLEDGMENTS

We acknowledge Kurt Adelberger for suggesting the IGM model used here. We thank Marc Kamionkowski, Avi Loeb, and Alice Shapley for helpful conversations.

## REFERENCES

- Adelberger K. L., Steidel C. C., Shapley A. E., Pettini M., 2003, *ApJ*, 584, 45
- Ajiki M., Taniguchi Y., Fujita S. S., et al., 2003, *AJ*, accepted, astro-ph/0307325
- Barger A. J., Cowie L. L., Capak P., Alexander D. M., Bauer F. E., Brandt W. N., Garmire G. P., Hornschemeier A. E., 2003, *ApJ*, 584, L61
- Barkana R., 2002, astro-ph/0212458
- Barkana R., Loeb A., 2003a, *Nature*, 421, 341
- Barkana R., Loeb A., 2003b, astro-ph/0305470
- Birnboim Y., Dekel A., 2003, *MNRAS*, accepted, astro-ph/0302161



Bond J. R., Cole S., Efstathiou G., Kaiser N., 1991, *ApJ*, 379, 440  
 Cen R., 2003a, *ApJ*, 591, L5  
 Cen R., 2003b, *astro-ph/0303633*  
 Chapman S. C., Blain A. W., Ivison R. J., Smail I. R., 2003, *Nature*, 422, 695  
 Charlot S., Fall S. M., 2000, *ApJ*, 539, 718  
 Ciardi B., Ferrara A., White S. D. M., 2003, *astro-ph/0302451*  
 Cole S., Lacey C. G., Baugh C. M., Frenk C. S., 2000, *MNRAS*, 319, 168  
 Fan X., Narayanan V. K., Strauss M. A., White R. L., Becker R. H., Pentericci L., Rix H., 2002, *AJ*, 123, 1247  
 Fan X., Strauss M. A., Schneider D. P., et al., 2003, *AJ*, 125, 1649  
 Fardal M. A., Katz N., Gardner J. P., Hernquist L., Weinberg D. H., Davé R., 2001, *ApJ*, 562, 605  
 Gnedin N. Y., 2000, *ApJ*, 535, 530  
 Haiman Z., 2002, *ApJ*, 576, L1  
 Haiman Z., Holder G. P., 2003, *ApJ*, submitted, *astro-ph/0302403*  
 Haiman Z., Spaans M., 1999, *ApJ*, 518, 138  
 Haiman Z., Spaans M., Quataert E., 2000, *ApJ*, 537, L5  
 Hu E. M., McMahon R. G., Cowie L. L., 1999, *ApJ*, 522, L9  
 Hu E. M., Cowie L. L., McMahon R. G., Capak P., Iwamuro F., Kneib J.-P., Maihara T., Motohara K., 2002a, *ApJ*, 568, L75  
 Hu E. M., Cowie L. L., McMahon R. G., Capak P., Iwamuro F., Kneib J.-P., Maihara T., Motohara K., 2002b, *ApJ*, 576, L99  
 Kennicutt R. C., 1998, *ARA&A*, 36, 189  
 Kodaira K. et al., 2003, *PASJ*, 55, L17  
 Kogut A. et al., 2003, *ApJ*, accepted, *astro-ph/0302213*  
 Kunth D., Mas-Hesse J. M., Terlevich E., Terlevich R., Lequeux J., Fall S. M., 1998, *A&A*, 334, 11  
 Lacey C., Cole S., 1993, *MNRAS*, 262, 627  
 Leitherer C. et al., 1999, *ApJS*, 123, 3  
 Loeb A., Rybicki G. B., 1999, *ApJ*, 524, 527  
 Miralda-Escude J., 1998, *ApJ*, 501, 15  
 Miralda-Escude J., Rees M. J., 1998, *ApJ*, 497, 21  
 Mo H. J., Mao S., White S. D. M., 1998, *MNRAS*, 295, 319  
 Neufeld D. A., 1991, *ApJ*, 370, L85  
 Osterbrock D.E., 1989, *Astrophysics of Gaseous Nebulae and Active Galactic Nuclei*. University Science Books, Sausalito, CA  
 Partridge R. B., Peebles P. J. E., 1967, *ApJ*, 147, 868  
 Peebles P.J.E., 1993, *Principles of Physical Cosmology*. Princeton University Press, Princeton, NJ  
 Reuland M. et al., 2003, *ApJ*, 592, 755  
 Rhoads J. E. et al., 2003, *AJ*, 125, 1006  
 Scannapieco E., Barkana R., 2002, *ApJ*, 571, 585  
 Schaerer D., 2003, *A&A*, 397, 527  
 Scott J., Bechtold J., Dobrzycki A., Kulkarni V. P., 2000, *ApJS*, 130, 67  
 Shapley A. E., Steidel C. C., Pettini M., Adelberger K. L., 2003, *ApJ*, 588, 65  
 Spergel D. N. et al., 2003, *ApJ*, accepted, *astro-ph/0302209*  
 Steidel C. C., Adelberger K. L., Shapley A. E., Pettini M., Dickinson M., Giavalisco M., 2003, *ApJ*, 592, 728  
 Taniguchi Y., Shioya Y., Fujita S. S., Nagao T., Murayama T., Ajiki M., 2003, *astro-ph/0306409*

Wyithe J. S. B., Loeb A., 2003, *ApJ*, 588, L69

This paper has been typeset from a  $\text{\TeX}$ / $\text{\LaTeX}$  file prepared by the author.